

SINGLE-AXIS LEVITATION EXPERIMENT (NASA)
65 p HC A04/MF A01

CSSL 22A

Unclas
G3/12 08350

NASA TECHNICAL MEMORANDUM

NASA TM-82447

ANALYSIS OF SPAR VIII SINGLE-AXIS LEVITATION EXPERIMENT

By J. E. Rush, C. F. Schafer, and R. L. Holland
Space Sciences Laboratory

September 1981

NASA



*George C. Marshall Space Flight Center
Marshall Space Flight Center, Alabama*

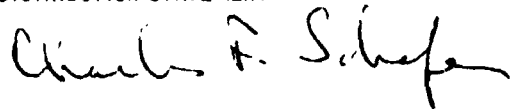
1. REPORT NO. NASA TM-82447		2. GOVERNMENT ACCESSION NO.		3. RECIPIENT'S CATALOG NO.	
4. TITLE AND SUBTITLE Analysis of SPAR VIII Single-Axis Levitation Experiment				5. REPORT DATE September 1981	
				6. PERFORMING ORGANIZATION CODE	
7. AUTHOR(S) J. E. Rush,* C. F. Schafer, and R. L. Holland				8. PERFORMING ORGANIZATION REPORT #	
9. PERFORMING ORGANIZATION NAME AND ADDRESS George C. Marshall Space Flight Center Marshall Space Flight Center, Alabama 35812				10. WORK UNIT NO.	
				11. CONTRACT OR GRANT NO.	
				13. TYPE OF REPORT & PERIOD COVERED Technical Memorandum	
12. SPONSORING AGENCY NAME AND ADDRESS National Aeronautics and Space Administration Washington, D.C. 20546				14. SPONSORING AGENCY CODE	
15. SUPPLEMENTARY NOTES Prepared by Space Sciences Laboratory, Science and Engineering Directorate *The University of Alabama in Huntsville					
16. ABSTRACT <p>The primary objectives of Experiment 74-42/2, which flew as part of the SPAR VIII payload on November 18, 1980, were melting and resolidification of a glass specimen in a containerless condition and the retrieval and examination of the specimen. The absence of container contact was to have been assured by use of a single-axis acoustic levitation system. However, the sample contacted a wire cage after being held without container contact by the acoustic field for only approximately 87 seconds. At this time, the sample was still molten and, therefore, flowed around the wire and continued to adhere to it. This report concentrates on an analysis of why the sample did not remain levitated free of container contact. The experiment is described, experimental observations are discussed and analyzed, and recommendations for future single-axis acoustic levitation experimentation are provided.</p>					
17. KEY WORDS Acoustic levitation Containerless processing			18. DISTRIBUTION STATEMENT  Unclassified-Unlimited		
19. SECURITY CLASSIF. (of this report) Unclassified		20. SECURITY CLASSIF. (of this page) Unclassified		21. NO. OF PAGES 64	22. PRICE NTIS

TABLE OF CONTENTS

	Page
I. EXPERIMENT DESCRIPTION	1
A. Objectives	1
B. Apparatus	1
C. Sample	5
D. Experiment Timeline	5
E. Data Collection	5
II. EXPERIMENTAL OBSERVATIONS	6
A. Primary Data	6
1. Film record	6
2. Accelerometer data	7
3. Angular rate data	7
4. Levitator data	14
B. Secondary Data	15
1. Digitized position data	15
2. Axial motion	16
3. Radial motion	16
4. Sample trajectory in the y-z plane	21
III. OBSERVED PHENOMENA REQUIRING EXPLANATION	21
IV. FORCES ACTING ON SAMPLE	23
V. ANALYSIS OF MOTION OF SPHERE	24
A. The Pressure Field	24
B. Orbit of the Sphere	27
C. Perturbations of the Orbit	31
1. Time-independent corrections to Hooke's law	31
2. Time-dependent force constant	32
3. Numerical analysis	33
4. Drag	35
5. Spin	37
6. Acoustic streaming	37
VI. SUMMARY AND CONCLUSIONS	40
A. Summary	40
B. Conclusions	40
C. Recommendations	41
REFERENCES	42
APPENDIX A	43
APPENDIX B	44
APPENDIX C	54
APPENDIX D	55

LIST OF ILLUSTRATIONS

Figure	Title	Page
1.	Acoustic levitator configuration showing extent of sample motion	2
2.	Acoustic potential well (radial, with shape factor b).....	3
3.	Acoustic levitator configuration for SPAR VIII.....	4
4.	SPAR R-19 science payload May 19, 1980, configuration	5
5.	SPAR project NIKE-BLACK Brant VC rocket mission profile, events and conditions.....	6
6.	Accelerometer A02	8
7.	Accelerometer A03	8
8.	Accelerometer A04	9
9.	Roll rate.....	9
10.	Pitch rate.....	10
11.	Yaw rate.....	10
12.	Rate of change of roll rate.....	12
13.	Rate of change of pitch rate.....	12
14.	Rate of change of yaw rate.....	13
15.	Acoustic driver voltage.....	14
16.	Acoustic driver current.....	14
17.	Acoustic driver phase.....	15
18.	Vibrator amplitude.....	15
19.	Vibrator temperature.....	15
20.	Axial motion of sample center.....	17
21.	Amplitude of axial oscillations as a function of time.....	17
22.	Axial period variation.....	18
23.	Axial position (100 frame averages).....	18
24.	Axial force constant variation (harmonic oscillator model).....	19

LIST OF ILLUSTRATIONS (Continued)

Figure	Title	Page
25.	Radial motion of sample center	19
26.	Radial amplitude variation.....	20
27.	Radial period variation.....	20
28.	Radial position (100 frame averages)	22
29.	Radial force constant variation (harmonic oscillator model).....	22
30.	Radial dependence of force in equilibrium plane.....	28
31.	Radial dependence of potential energy function in equilibrium plane.....	28
32.	Axial dependence of potential - energy function.....	29
33.	Axial dependence of force.....	29
34.	Calculated sample orbit	34
35.	Projection of calculated orbit onto a line	34
36.	Projection of calculated orbit onto a line	36
37.	Sample orbit.....	36
B-1.	Sample trajectory for time $t = 4.21$ to 8.34 sec.....	44
B-2.	Sample trajectory for time $t = 8.38$ to 12.50 sec.....	44
B-3.	Sample trajectory for time $t = 12.55$ to 16.68 sec.....	45
B-4.	Sample trajectory for time $t = 16.72$ to 20.81 sec.....	45
B-5.	Sample trajectory for time $t = 20.85$ to 24.98 sec.....	46
B-6.	Sample trajectory for time $t = 25.02$ to 29.15 sec.....	46
B-7.	Sample trajectory for time $t = 25.71$ to 29.84 sec.....	47
B-8.	Sample trajectory for time $t = 29.88$ to 34.01 sec.....	47
B-9.	Sample trajectory for time $t = 35.05$ to 38.18 sec.....	48
B-10.	Sample trajectory for time $t = 38.22$ to 42.35 sec.....	48
B-11.	Sample trajectory for time $t = 42.39$ to 46.52 sec.....	49

LIST OF ILLUSTRATIONS (Concluded)

Figure	Title	Page
B-12.	Sample trajectory for time $t = 46.56$ to 50.69 sec.....	49
B-13.	Sample trajectory for time $t = 50.73$ to 54.86 sec.....	50
B-14.	Sample trajectory for time $t = 54.98$ to 59.03 sec.....	50
B-15.	Sample trajectory for time $t = 59.07$ to 63.20 sec.....	51
B-16.	Sample trajectory for time $t = 63.24$ to 67.37 sec.....	51
B-17.	Sample trajectory for time $t = 67.41$ to 71.54 sec.....	52
B-18.	Sample trajectory for time $t = 71.58$ to 75.71 sec.....	52
B-19.	Sample trajectory for time $t = 75.75$ to 79.88 sec.....	53
B-20.	Sample trajectory for time $t = 79.92$ to 84.05 sec.....	53
D-1.	Average radial position as a function of time	56
D-2.	Average axial position as a function of time	56
D-3.	Apparent radial force	58
D-4.	Apparent axial force	58

TECHNICAL MEMORANDUM

ANALYSIS OF SPAR VIII SINGLE-AXIS LEVITATION EXPERIMENT

I. EXPERIMENT DESCRIPTION

A. Objectives

Experiment 74-42/2, which flew as a part of the Space Processing Applications Rocket (SPAR) VIII payload on November 18, 1980, had as primary objectives the melting and resolidification of a glass specimen in a containerless condition, and the retrieval and examination of the specimen. The absence of container contact was to have been assured by use of a single-axis acoustic levitation system designed and built by Intersonics, Inc. The experimental objectives were degraded by two events. First, the sample contacted a wire cage after being held without container contact by the acoustic field for only approximately 87 sec. At this time, the sample was still molten and therefore flowed around the wire and continued to adhere to it. Second, the sample was lost (and probably destroyed) because of failure of a parachute and the resulting crash of the SPAR payload. We will concentrate here on analysis aimed at the first problem; that is, why the sample did not remain levitated free of container contact.

B. Apparatus

The single-axis acoustic levitation system consists essentially of an acoustic generator and amplifier which drive linear oscillations of a cylinder. The circular area forming the cylinder end oscillates in a direction parallel to the cylinder axis, producing sound waves which are reflected by a circular plate which is co-axial with the driving cylinder (Fig. 1). The reflected sound wave interferes with the primary wave, producing a three-dimensional pressure field which ideally has cylindrical symmetry about the cylinder axis. This pressure field has minima at nodal points along the cylinder axis which correspond to the bottoms of three-dimensional potential wells. An object placed in the field will move to the center of the well or oscillate around or through it depending on the initial momentum and on the absence of other dominant forces. Figure 2 shows qualitatively the shape of these potential wells. The potential is generally considered very nearly of the form $1/2Kr^2$ for the radial dependence and $1/2Kz^2$ for the axial dependence. That is, in this approximation, the motion of a levitated object (neglecting other forces) can be described in terms of superposition of two independent motions. One of these is a simple harmonic oscillation parallel to the z-direction. The other is motion due to a central force of magnitude Kr . This motion can be straight line, circular, or elliptical depending on initial conditions. The details of these motions and the nature of deviations from them will be discussed in depth in this report.

The configuration for Experiment 74-42/2 is shown in Figure 3. In addition to the sound source and reflector which produce the levitating field, there are heater rods around the volume occupied by the sample which provide the heat

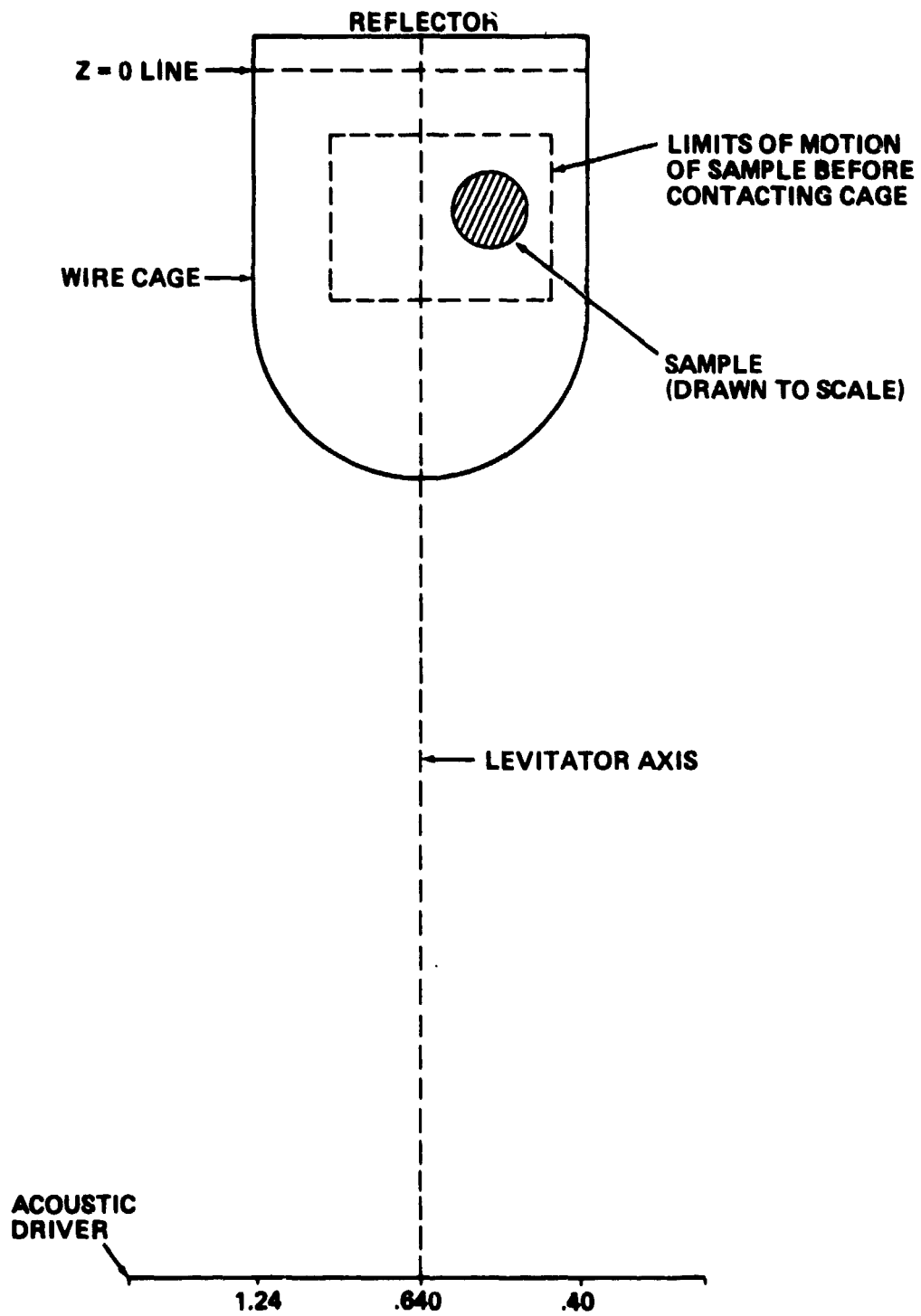


Figure 1. Acoustic levitator configuration showing extent of sample motion.

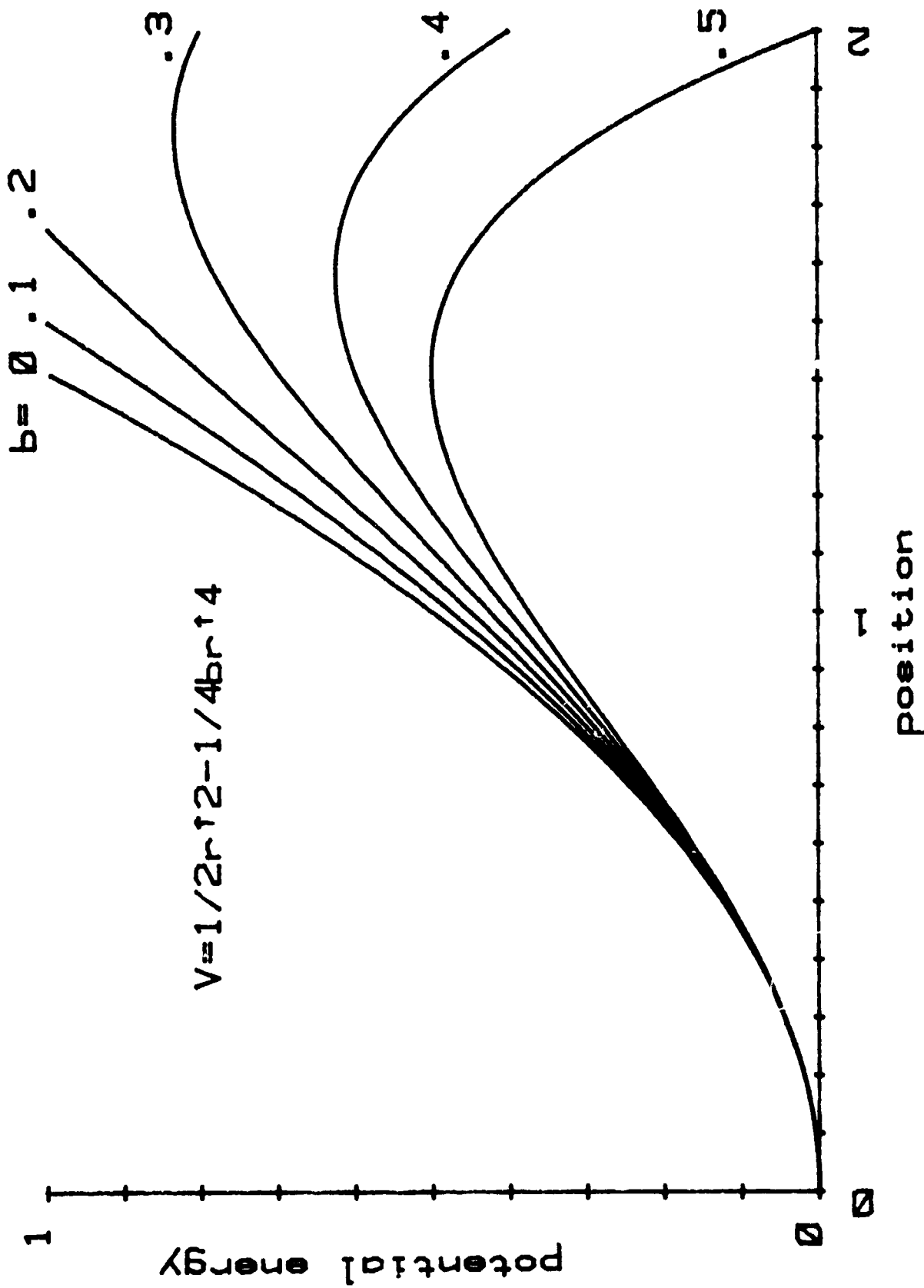


Figure 2. Acoustic potential well (radial, with shape factor b).

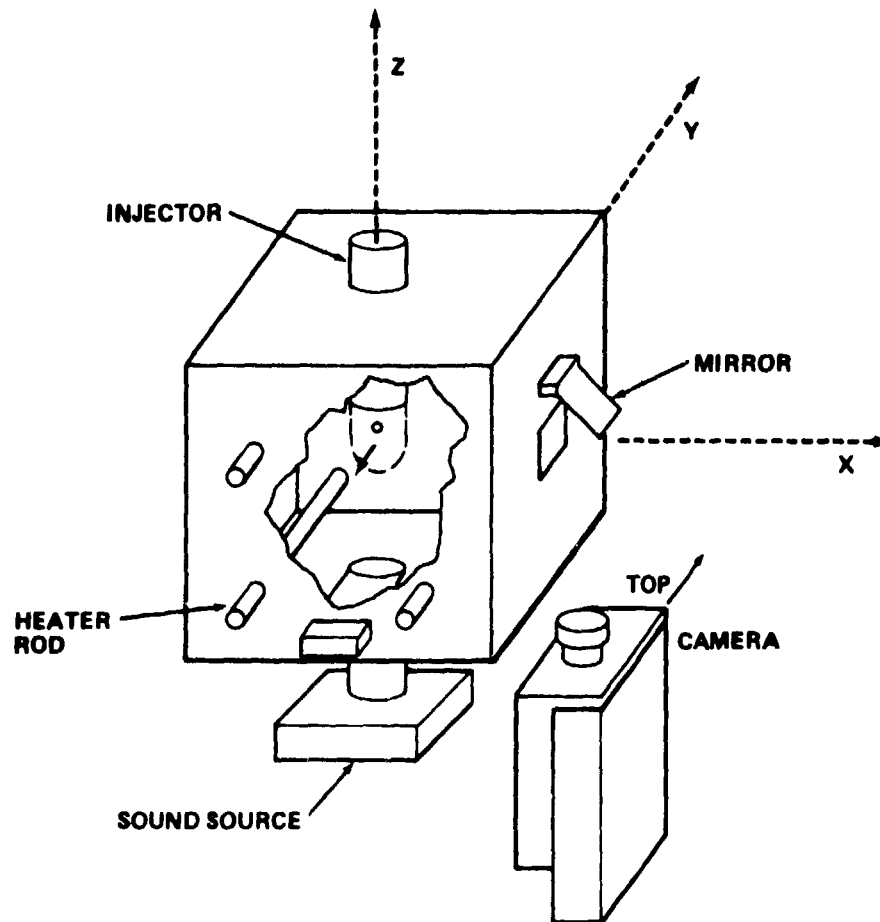


Figure 3. Acoustic levitator configuration for SPAR VIII.

necessary to melt the sample. There is an injection system consisting of a springloaded cage designed to hold the sample motionless against the reflector for protection during launch. At the beginning of the experiment, the cage is moved along the z-axis so the sample is free to move without contact with any container. After processing, the cage is designed to retract (moving in the +z-direction) so that the sample is recaptured and held motionless during re-entry and impact. There is an optical system, consisting of a mirror and a motion picture camera, for observation of the sample during the course of the experiment.

The experiment package is mounted on the front end of the SPAR payload (Fig. 4). The entire 74-42/2 package is within less than 2 of the payload center of mass. (The payload center of mass is designed to be on the z-axis and near the geometric center of the payload.) The orientation of the experiment is shown in Figure 3. The axis of the levitator (geometric axis through the center of driver and reflector) is parallel to the spacecraft z-axis. The camera mounting arrangement produces a view in which the positive y-direction is up and the positive z-direction is to the right. That is, although the image produced of the sample is of the side toward the positive x-direction, the motion observed is that which would be seen by looking along the x-axis from - to + with +y upward. In addition, Intersonics, Inc., reported that the camera was rotated by approximately 6 degrees in its mounting so that in image, the levitator acoustic axis would appear to be rotated counterclockwise by approximately 6 degrees.

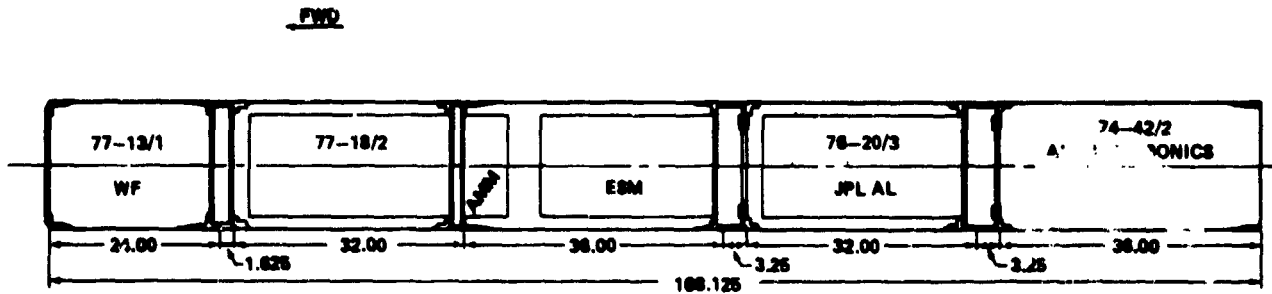


Figure 4. SPAR R-19 science payload May 19, 1980, configuration.

C. Sample

The sample processed in the Intersonics levitator and furnace system was reported by Dr. Ralph Happe of Rockwell (the Principal Investigator) to be a gallia(41%)-calcia(36%)-silica(23%) sphere having a mass of 0.595 gm. Measurements of neither diameter nor density were available for the flight sample. However, using the molar fraction concentrations given by Dr. Happe and the Handbook of Chemistry and Physics (50th Edition) values for densities of gallia, calcia, and silica, a density of 4.43 gm/cm^3 was computed (see Appendix A). This yields a value of the sphere diameter of 0.635 cm (0.250 in.).

D. Experiment Timeline

Figure 5 shows the planned experiment timeline superimposed on the SPAR trajectory. The experiment functioned as planned until the sample contacted the wire cage after approximately 87 sec of experiment time (launch +204 sec).

E. Data Collection

The SPAR acoustic single-axis levitation experiments yielded data of four separate types. First, a 16 mm motion picture camera recorded visual observations of the motion of the sample sphere in the levitator from sphere injection throughout the heating and cooling phases of the experiment. Second, a three-axis accelerometer (on SPAR VIII) allowed monitoring of linear accelerations at the accelerometer positions throughout the low-g phase of the flight. Third, a rate gyro system provided continuous monitoring of angular rates about roll, pitch, and yaw axes. Fourth, housekeeping data for the experiment were provided continuously. These included measurements of acoustic driver voltage, current, and phase as well as vibrator amplitude and temperature.

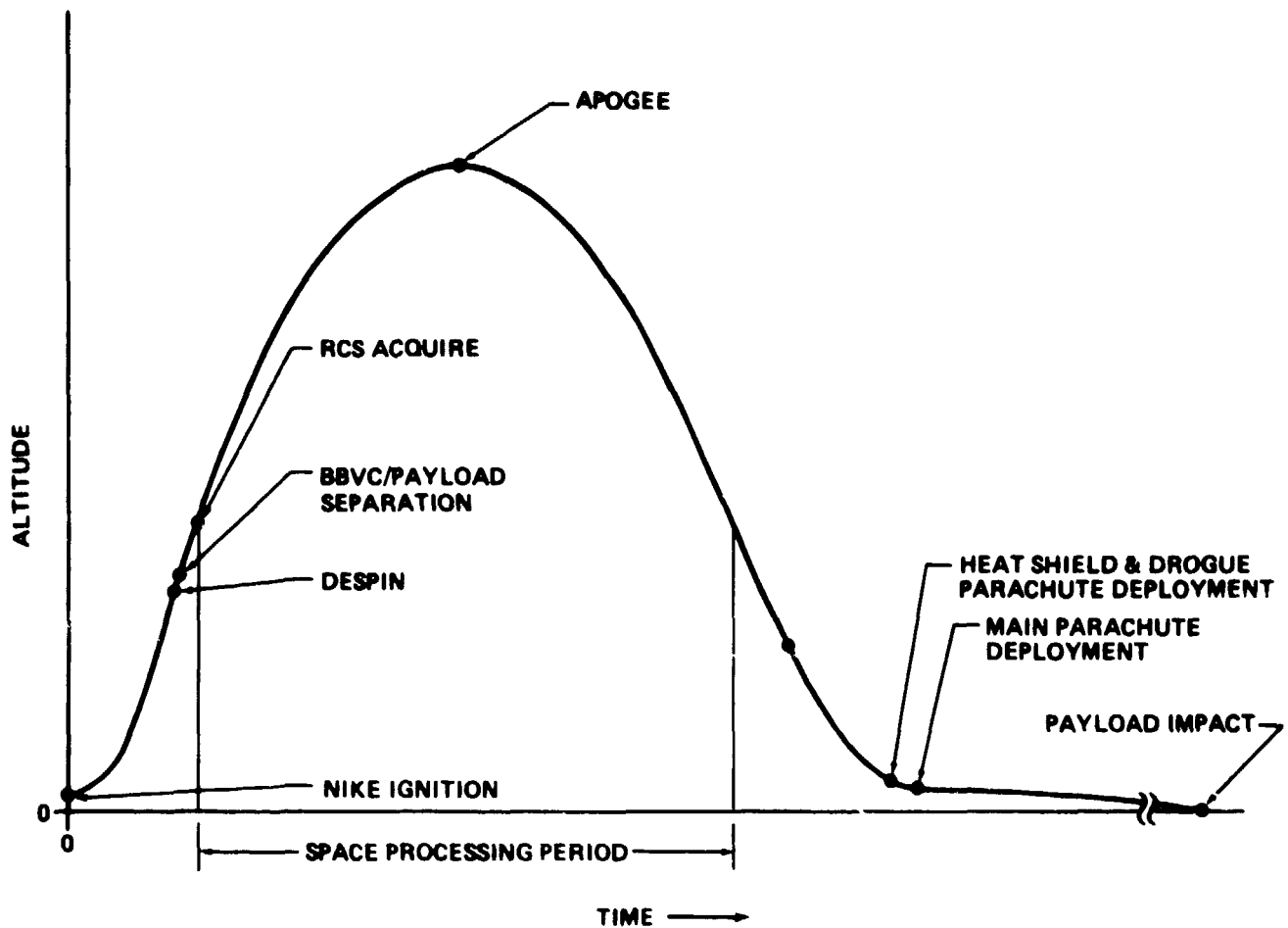


Figure 5. SPAR project NIKE-BLACK Brant VC rocket mission profile, events and conditions.

II. EXPERIMENTAL OBSERVATIONS

A. Primary Data

1. Film Record.

The motion picture record of the experiment shows the sphere in the cage assembly prior to injection into the levitating acoustic field. Injection is observed at the expected time. The sphere then is seen to develop a rotational motion about an axis internal to the sphere. This rotation appears to build up to a rate which becomes comparable to the camera frame rate (24 frames per sec). This fact, coupled with low contrast between sample and background, makes the observation of sample spin rather qualitative.

The sample is also seen to begin an oscillatory motion which has components in the direction of the levitator axis and along a levitator radius. Since only one

camera view is available, we are able to observe only a projection of the sample motion onto the camera viewing plane. This oscillatory motion is observed to persist for approximately 87 sec after sample injection. Drifts are observed in the apparent centers of motion both axially and radially during this 87-sec period. At the end of this period the sample is observed to move abruptly a short distance (about a sample radius) and then come to rest, apparently adhering to the sample cage. The sample was molten at that time and appeared to have flowed around one of the cage wires and centered itself on the wire.

2. Accelerometer Data.

The three-axis accelerometer records are shown in Figures 6 through 8. The A02 record indicates an oscillatory behavior of that component of acceleration having an amplitude no greater than approximately 1.5×10^{-5} g. These oscillations are about a steady background level of approximately -5×10^{-6} g. Assuming that the zero calibration of the accelerometer represents zero gravity, the excursions of measured acceleration levels for A02 lie between approximately 1×10^{-5} g and -2×10^{-5} g. It is likely that the measured steady component at -5×10^{-6} g represents a zero reading from the instrument. This would imply that acceleration levels fluctuated between approximately $+1.5 \times 10^{-5}$ g and -1.5×10^{-5} g. Whichever interpretation represents the real situation, the magnitude of observed acceleration levels for A02 never exceeds approximately 2×10^{-5} g. Accelerometer A03 recorded a mean background acceleration level of approximately -1.5×10^{-5} g with maximum fluctuations about this level of approximately $\pm 2.5 \times 10^{-5}$ g. Assuming again that the accelerometer zero level is unshifted, the range of acceleration excursions in this direction is approximately $+1.0 \times 10^{-5}$ g to -4.0×10^{-5} g. If the -1.5×10^{-5} g reading indicates the zero acceleration level, then the range is $+2.5 \times 10^{-5}$ g to -2.5×10^{-5} g. Accelerometer A04 indicates a background acceleration level which decays from approximately 1.0×10^{-5} g to approximately -0.2×10^{-5} g over the low-g phase of the flight. Maximum excursions from this mean are approximately $\pm 1.5 \times 10^{-5}$ g. Assuming zero shift in accelerometer calibration, accelerations in this direction lie within the limits $+3.0 \times 10^{-5}$ g to -2.5×10^{-5} g.

3. Angular Rate Data.

Data are available for SPAR VIII from the payload's rate gyro system giving rotation rates about roll, pitch, and yaw axes (Figs. 9 through 11). Rotations about each of these yaw axes can potentially give rise to accelerations of the sample in at least two different ways. First, centrifugal accelerations can arise due to the rate of change of angular position according to

$$\bar{\omega} \times \bar{r} = \bar{a}_c.$$

This can be broken down into motion about each of these independent axes (yaw, pitch, and roll). We will have then:

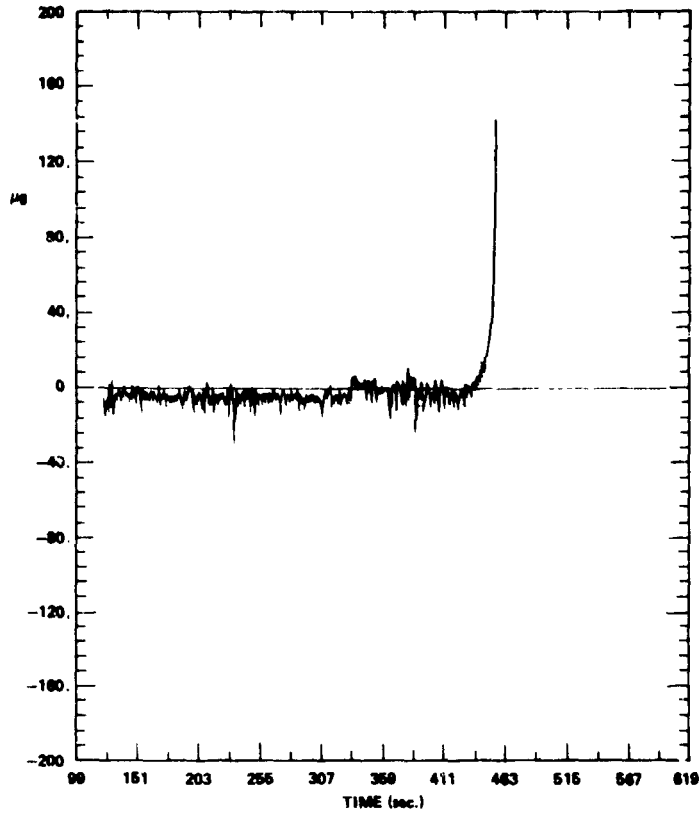


Figure 6. Accelerometer A02.

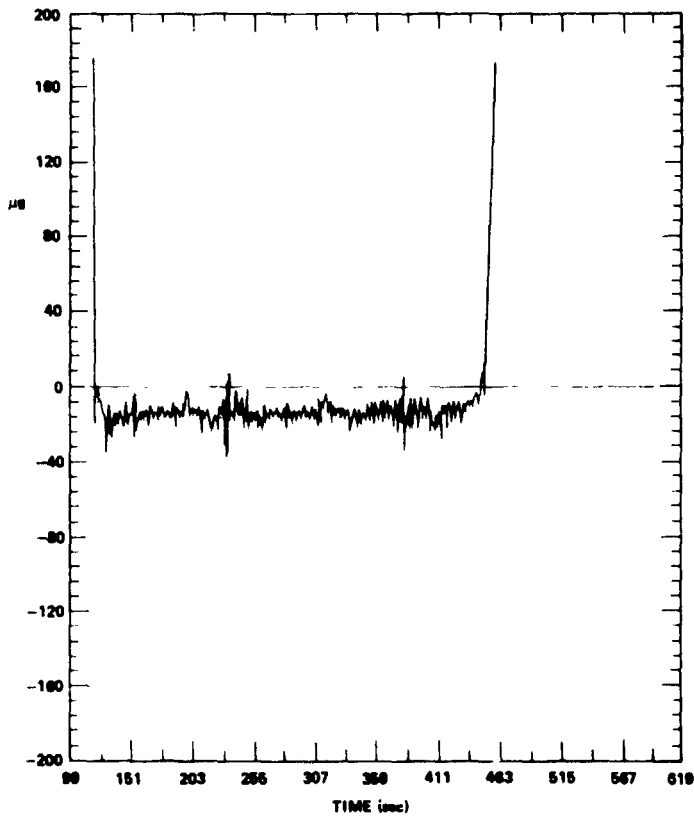


Figure 7. Accelerometer A03.

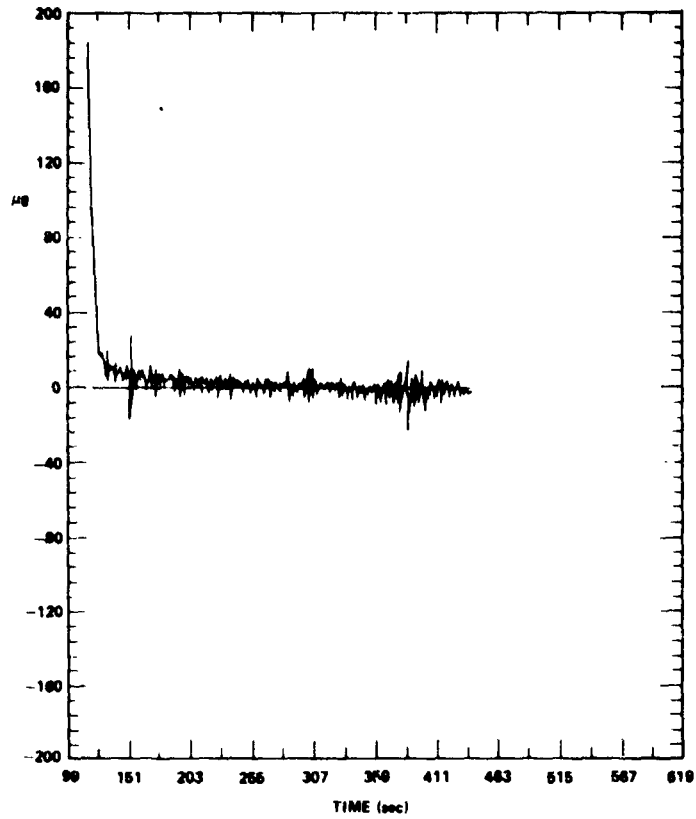


Figure 8. Accelerometer A04.

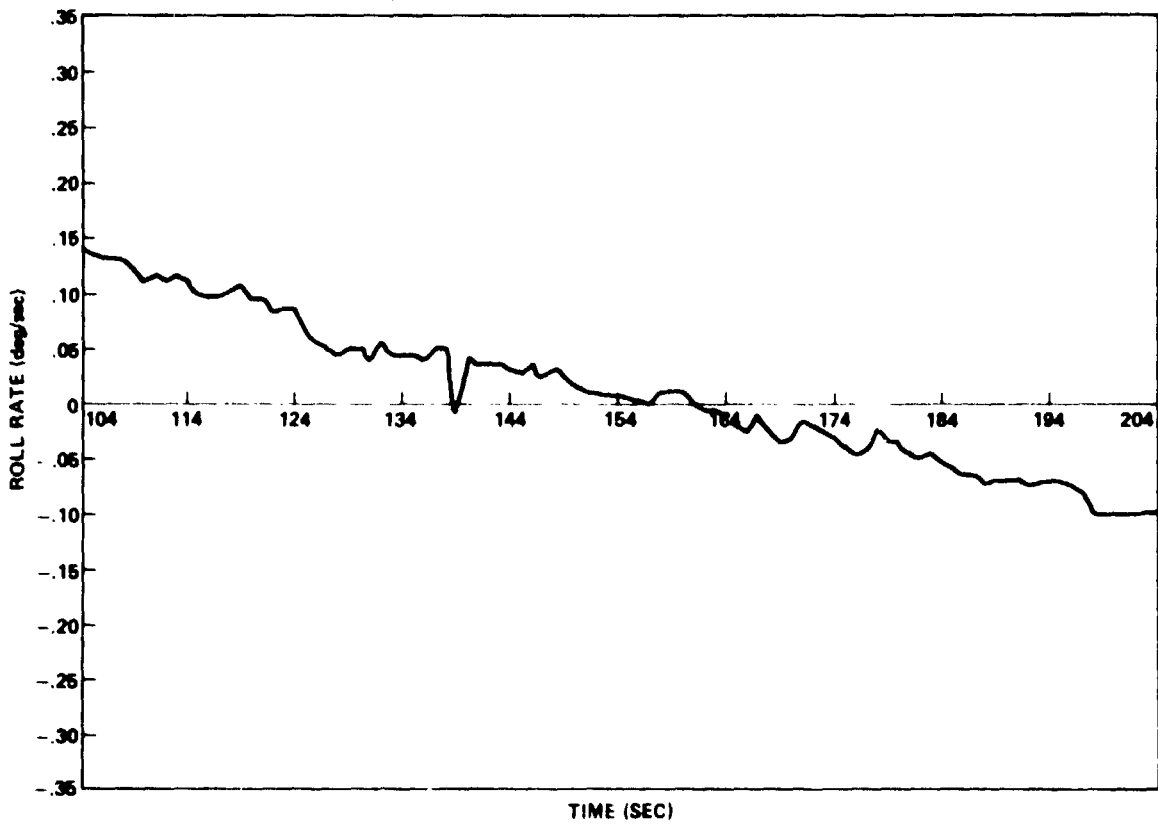


Figure 9. Roll rate.

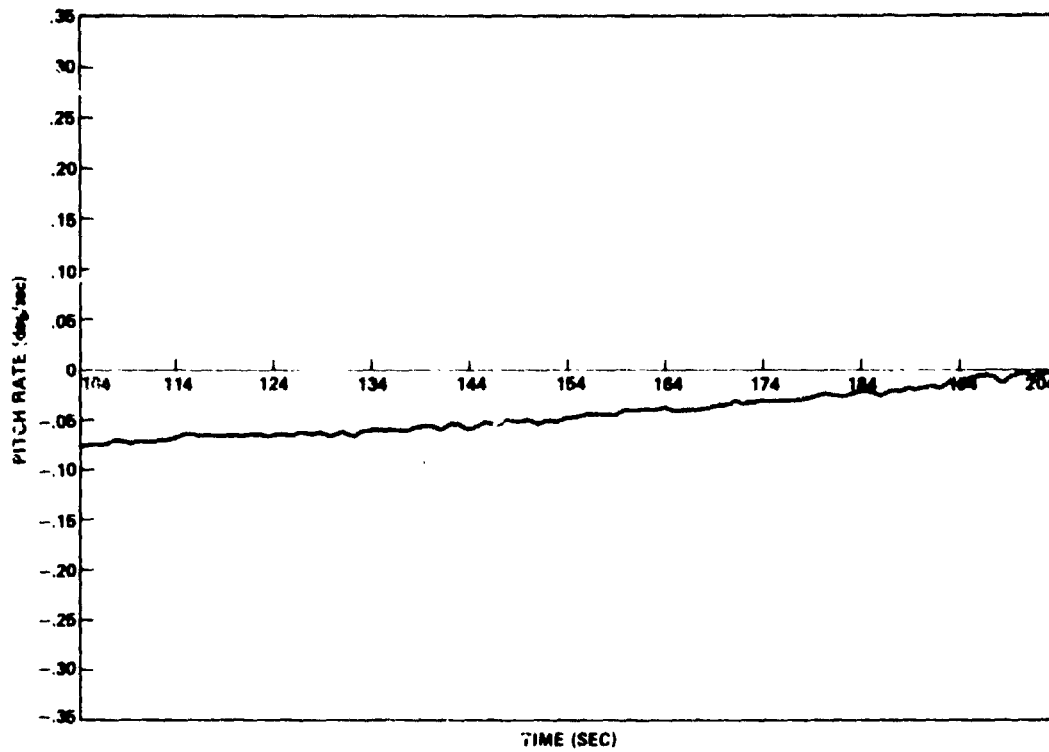


Figure 10. Pitch rate.

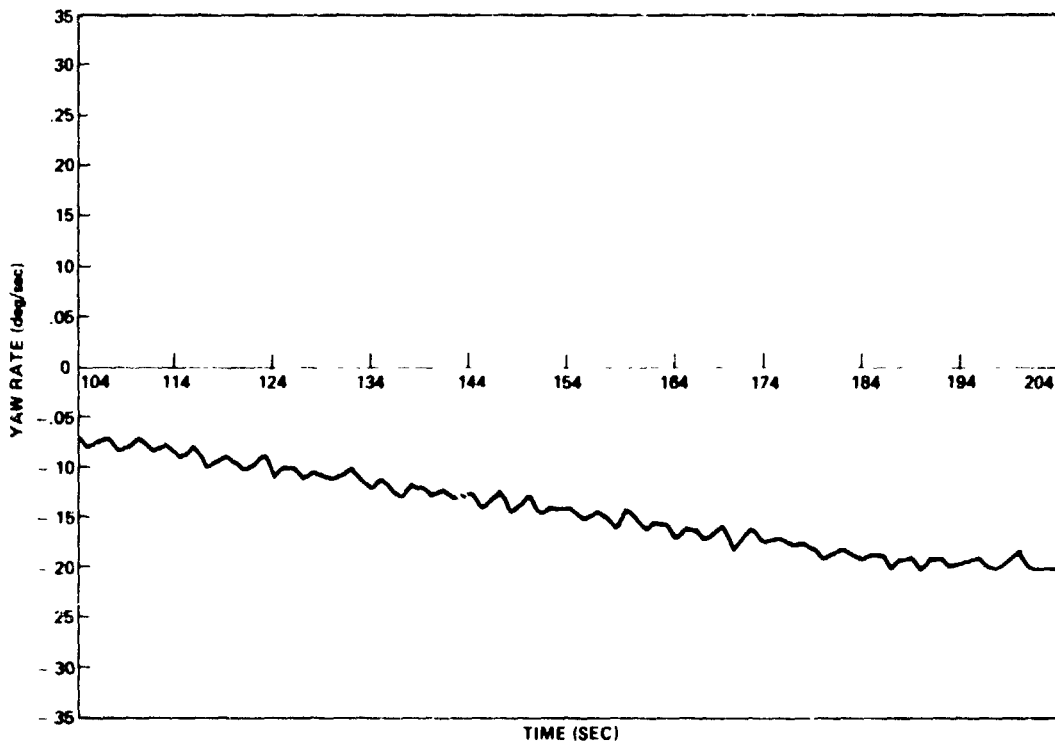


Figure 11. Yaw rate.

$$\omega_p^2 r_{pe} = a_{pe}$$

$$\omega_r^2 r_{re} = a_{re}$$

$$\omega_y^2 r_{ye} = a_{ye}$$

where ω_p , ω_r , and ω_y are rotations about the pitch, roll, and yaw axes respectively; r_{pe} , r_{re} , and r_{ye} are distances from the pitch, roll, and yaw axes to the experiment location; and a_{pe} , a_{re} , and a_{ye} are acceleration components experienced by a sample at the experiment location. These accelerations are directed outward from the rotation axes.

In addition, there are accelerations which arise due to changes in the rotation rates. These accelerations are of the form:

$$\bar{b} = \dot{\omega} \times \bar{r}.$$

Components of this acceleration will have the following magnitudes:

$$\dot{\omega}_p r_{pe} = b_{pe}$$

$$\dot{\omega}_r r_{re} = b_{re}$$

$$\dot{\omega}_y r_{ye} = b_{ye}.$$

where $\dot{\omega}_p$, $\dot{\omega}_r$, $\dot{\omega}_y$ are the time rates of change of rotation rate about the roll, pitch, and yaw axes respectively (Figs. 12 through 14); and b_{pe} , b_{re} , b_{ye} are the components of acceleration experienced by a sample at the experiment location due to rates of change of rotation about the respective axes. The accelerations here are directed perpendicularly to the rotation axis and to the radius from the given axis out to the experiment.

The flight data must be examined to determine acceleration levels induced by residual spacecraft motion. The levitated sample was lost after less than 100 sec of experiment time, which fell within the period $t = 104$ sec to $t = 204$ sec on the experiment timeline. Good angular data exist for this period, so the required analysis is possible. During this period, roll rates began at $-0.14^\circ/\text{sec}$, went through 0, and climbed to $+0.05^\circ/\text{sec}$. The maximum value (absolute value) of roll rate was $0.14^\circ/\text{sec}$. The average rate of change of roll rate over this period was $0.0021^\circ/\text{sec}^2$. Pitch rates ranged from a beginning value of $-0.07^\circ/\text{sec}$ to $0^\circ/\text{sec}$ at 204 sec. Maximum absolute value was $0.07^\circ/\text{sec}$. Average rate of change of pitch

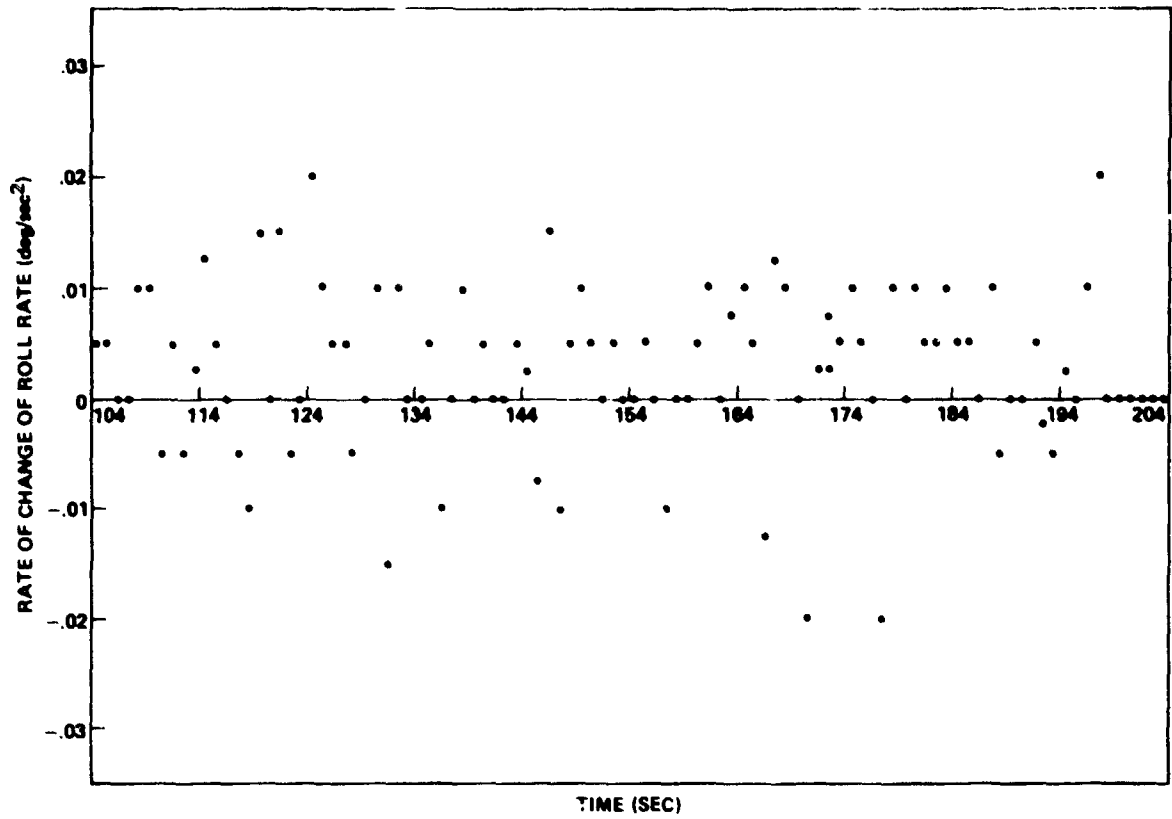


Figure 12. Rate of change of roll rate.

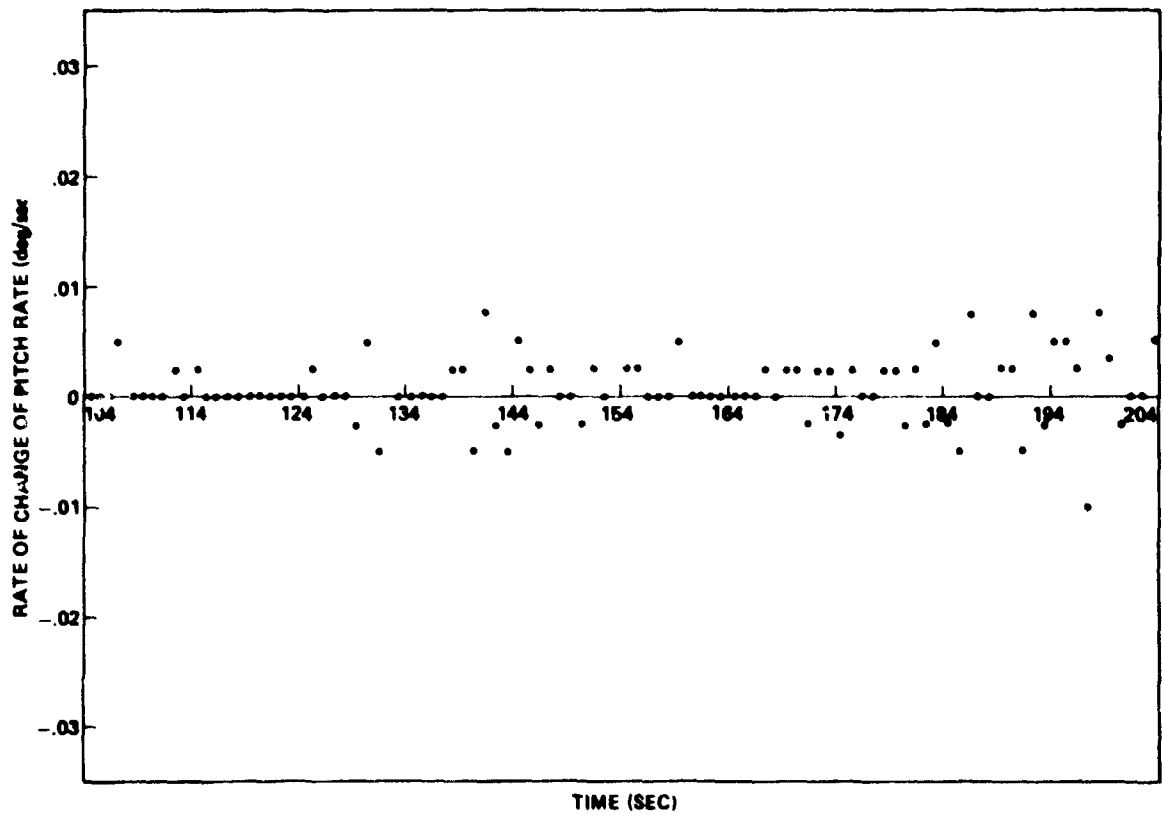


Figure 13. Rate of change of pitch rate.

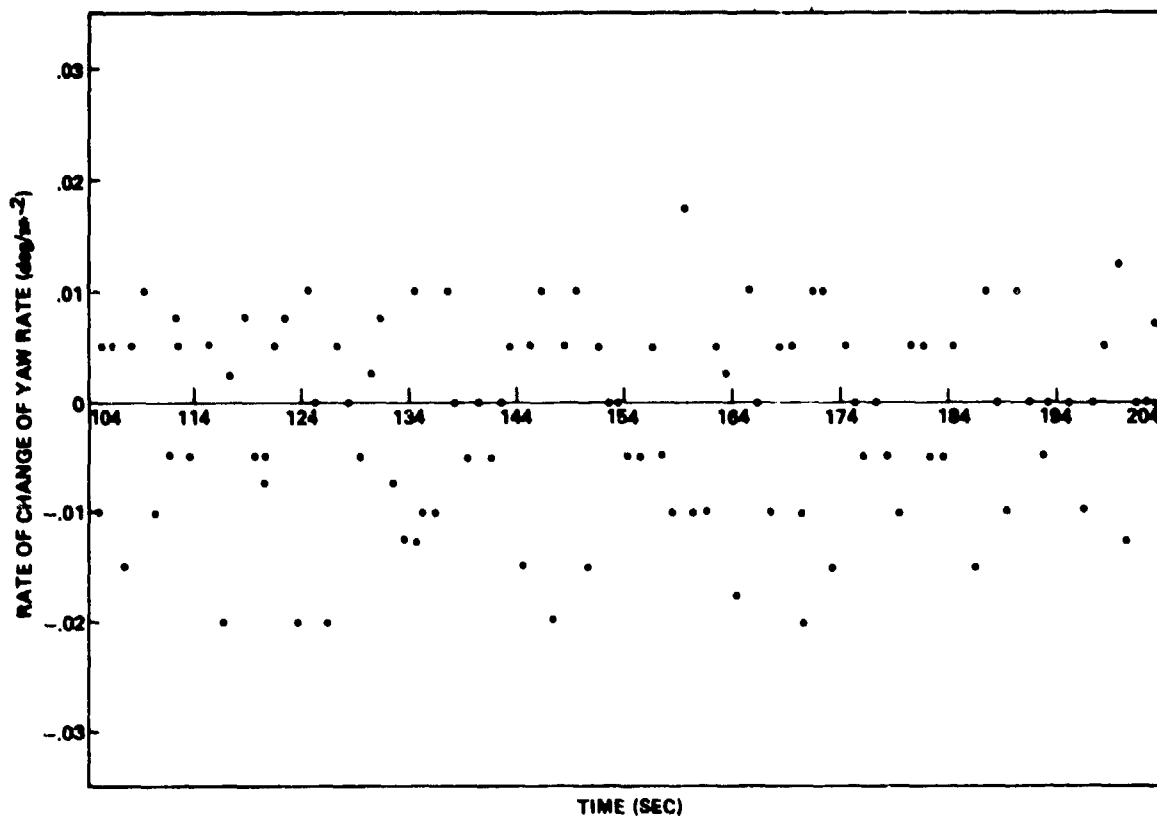


Figure 14. Rate of change of yaw rate.

rate was $0.0007^\circ/\text{sec}^2$. The yaw rate ranged from an initial $-0.07^\circ/\text{sec}$ to a final rate (at $t = 204$ sec) of $-0.2^\circ/\text{sec}$. Maximum absolute value of yaw rate was $0.2^\circ/\text{sec}$. Average rate of change of yaw rate was $0.0013^\circ/\text{sec}^2$. None of the angular rate changes varied greatly from linearity with time.

Experiment distances from the roll axis are on the order of 0.1 m. Distances from the yaw and pitch axes are less than 2 m. These values can be used to place upper limits on the magnitudes of accelerations experienced by a sample at the experiment location due to $\dot{\omega}$ and $\ddot{\omega}$.

$$a_{re} = 5.8 \times 10^{-8} \text{ g}$$

$$a_{pe} = 2.9 \times 10^{-7} \text{ g}$$

$$a_{ye} = 2.5 \times 10^{-6} \text{ g.}$$

a_{re} and a_{ye} are in the same direction, but their combined effect is still on the order of 10^{-6} g.

$$b_{re} = 3.7 \times 10^{-7} \text{ g}$$

$$b_{pe} = 2.5 \times 10^{-6} \text{ g}$$

$$b_{ye} = 4.6 \times 10^{-6} \text{ g}$$

These acceleration levels are all too small by at least two orders of magnitude to have any significant effect on the motion of the levitated sample.

4. Levigator data.

Figures 15 through 19 show levigator housekeeping data. These data indicate that the levitation system acoustic output was normal throughout the experiment and that the vibration temperature was within allowable limits. It can be inferred from this that electrically and mechanically the acoustic driver and vibrator functioned normally. The loss of sample by drifting into the cage then was caused by some other factor or factors.

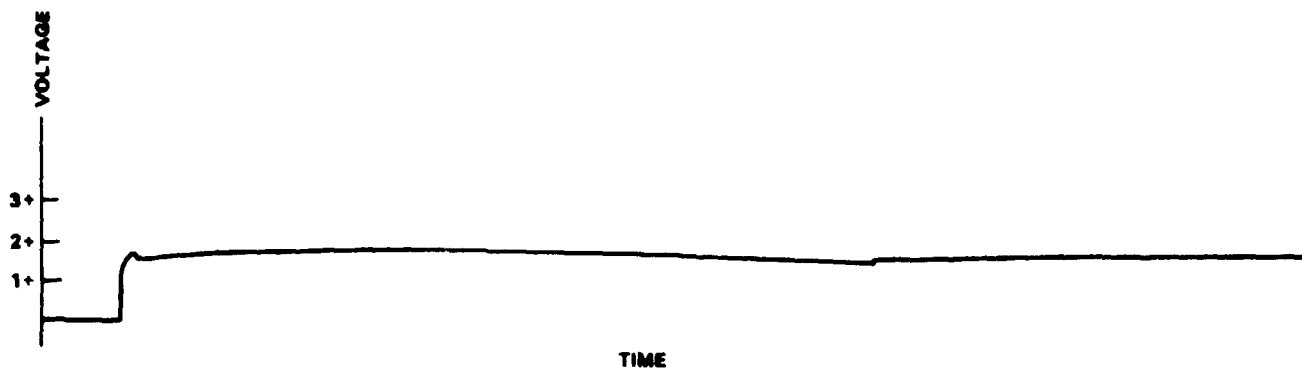


Figure 15. Acoustic driver voltage.

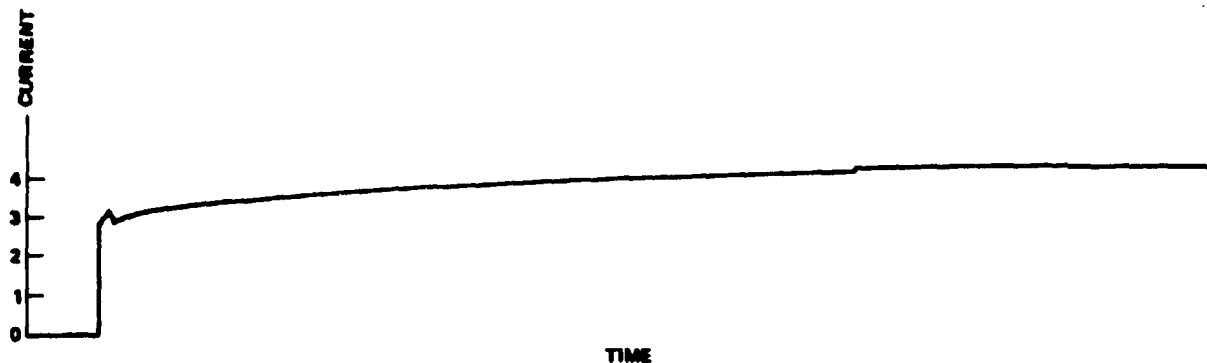


Figure 16. Acoustic driver current.

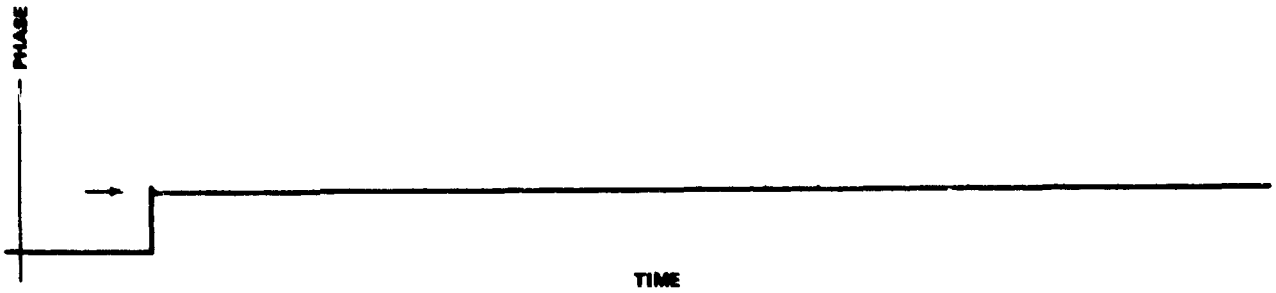


Figure 17. Acoustic driver phase.

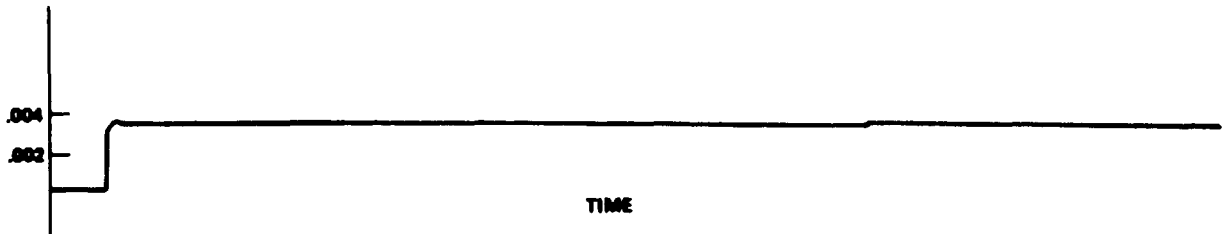


Figure 18. Vibrator amplitude.



Figure 19. Vibrator temperature.

B. Secondary Data

1. Digitized position data.

The motion picture film of the SPAR VIII experiment was analyzed frame by frame to obtain a record of the projection of the sample trajectory onto the film plane. This set of measurements from the film was done by Intersonics, Inc. The data were compiled in tabular form showing frame number and sample coordinates

(right, left, top, and bottom sample edge positions were shown). This tabulated data set was provided to the Marshall Space Flight Center Space Sciences Laboratory for analysis. Here the data were transferred to magnetic tape so that data presentation and analysis could be more readily accomplished. All the position data discussed later were plotted from this tabulated data set.

In the simplest approximation to the sample motion, the two-dimensional projection of the three-dimensional sample trajectory provides a fairly complete description of the sample motion. As noted previously, the motion in this approximation can be described by an axial (z-direction) simple harmonic motion superposed on a central force motion [with $V(r) = 1/2 Kr^2$]. The radial motion can further be described by a superposition of two linear harmonic oscillators with the same force constant K. A measurement of the period of any projection of the radial motion onto a line is then sufficient to calculate the force constant. Details of the actual trajectory, i.e., $x(t)$ and $y(t)$, are not interesting in this approximation for this application and would require knowledge of $x(t_0)$ and $y(t_0)$, where t_0 is any value of time (initial condition).

It was observed in the analysis of SPAR VIII experimental results that the motion of the sample in the acoustic field does not follow exactly this simple harmonic oscillator description. The deviations from this model are both interesting and critical to the outcome of the experiment. The use of a single-view camera system is adequate when the motion is near simple harmonic, but information about sample behavior (hence about the nature of the acoustic field) is lost when deviations from this motion are significant. The use of an optical system which provides projections of the motion on two perpendicular planes would permit a frame by frame plot of sample trajectory which would allow calculations of acoustic forces (magnitude and direction) as a function of time.

2. Axial motion.

Figure 20 shows a plot of the projection of the sample motion onto the z-axis. The motion is seen to be cyclic with a varying amplitude and period and with a net drift in the mean sample position. Figure 21 shows the amplitude of the axial oscillation as a function of time. Time variation of the period of the axial oscillation over the duration of the experiment is shown in Figure 22. A plot of average axial position with time gives a direct indication of drift of the axial "center of motion" or "equilibrium position". This is shown in Figure 23.

Using simple harmonic oscillator approximation to the axial motion, an approximate force constant can be extracted from the sample period as a function of time (from $\omega = 2\pi/T = \sqrt{k/m}$). Axial force constant, in this approximation, is shown in Figure 24. As indicated elsewhere, this approximation is not adequate for a full description of sample behavior, but does serve to provide a lowest order description.

3. Radial motion.

Sample radial motion—that is, the projection of motion in the x-y plane onto a line in that plane (perpendicular to the camera viewing direction)—is shown in Figure 25. The radial motion shows some of the characteristics of the axial motion. That is, there is an oscillatory motion which varies in amplitude and frequency over the duration of the experiment; and there is a drift in the average sample position. The amplitude of the radial oscillations as a function of time is shown in Figure 26.

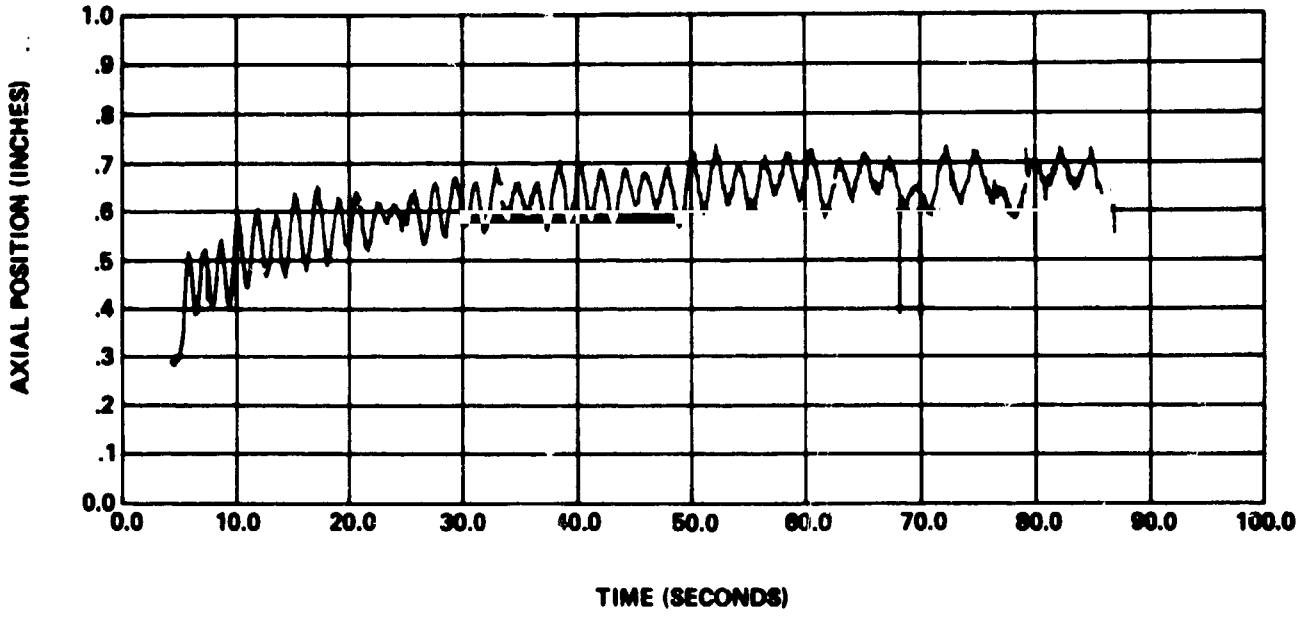


Figure 20. Axial motion of sample center.

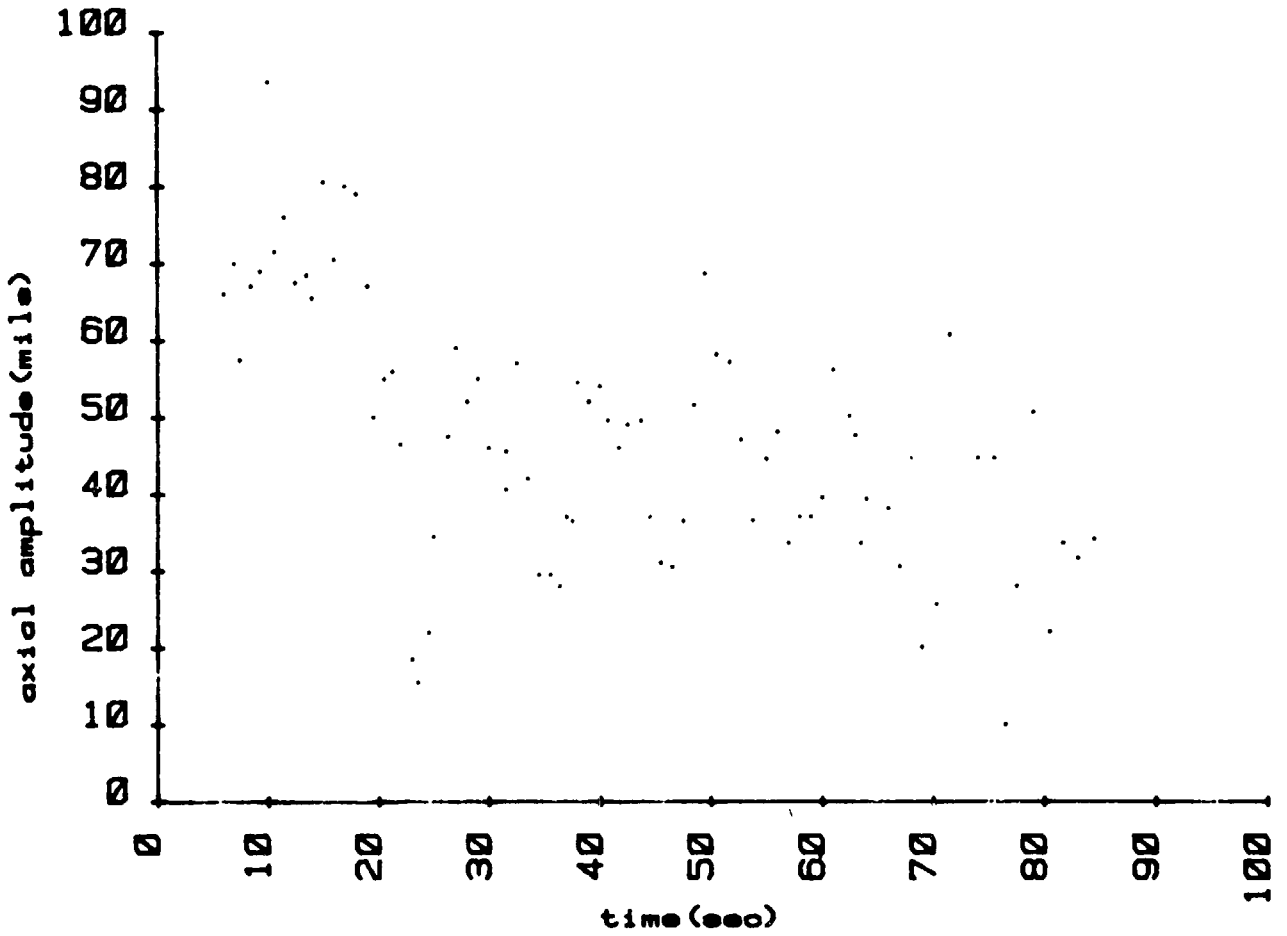


Figure 21. Amplitude of axial oscillations as a function of time.

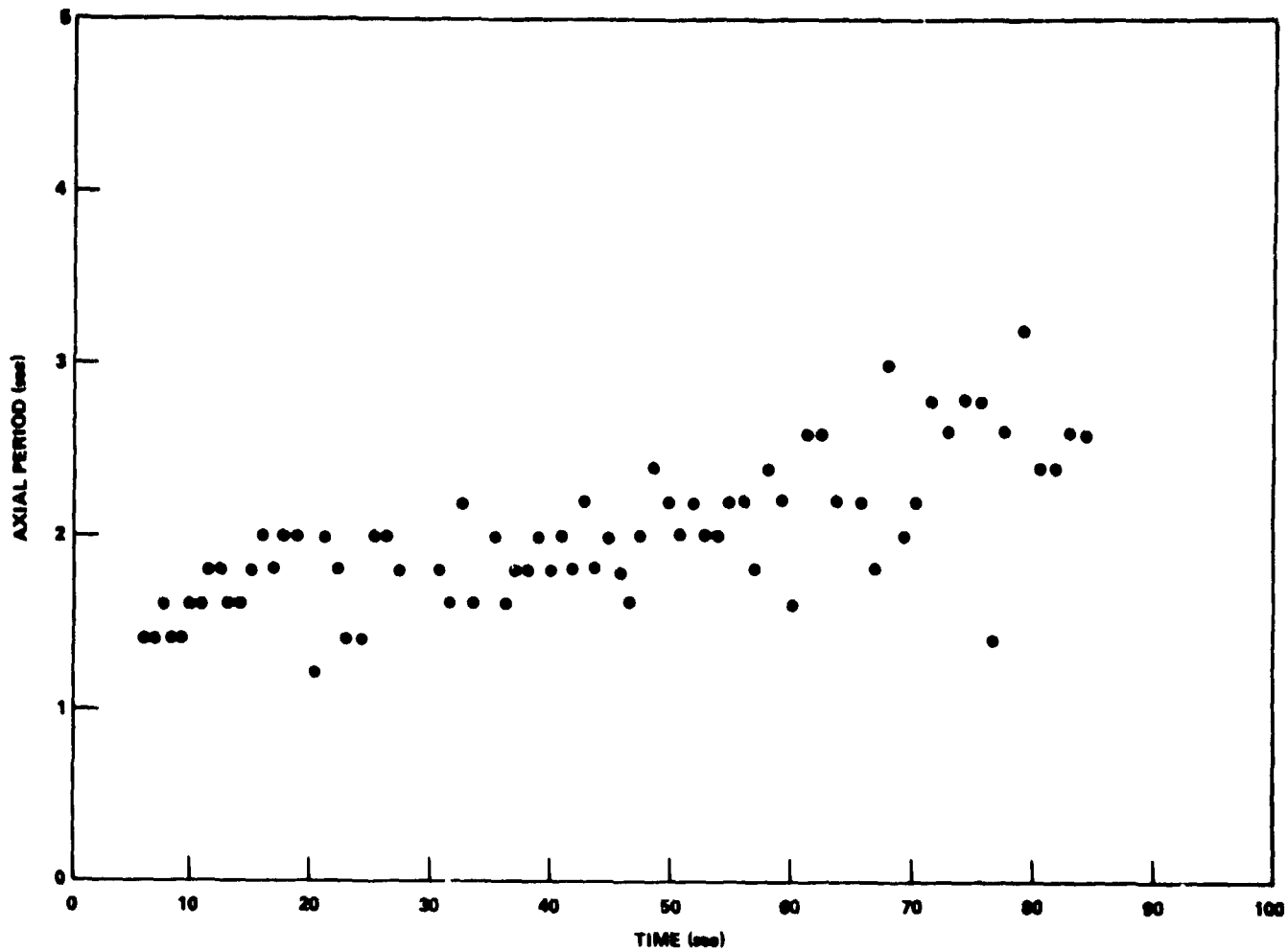


Figure 22. Axial period variation.

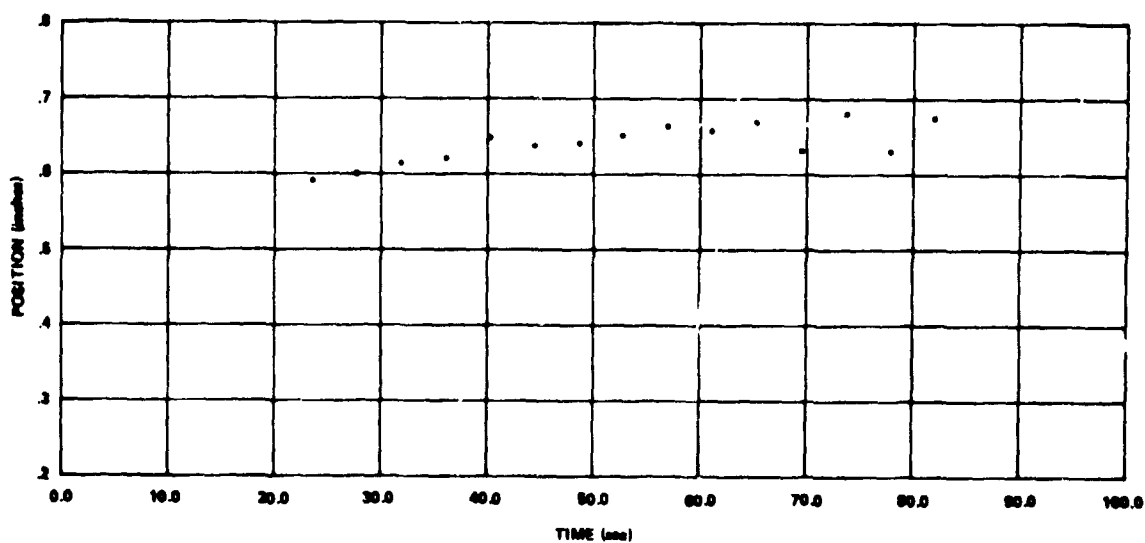


Figure 23. Axial position (100 frame averages).

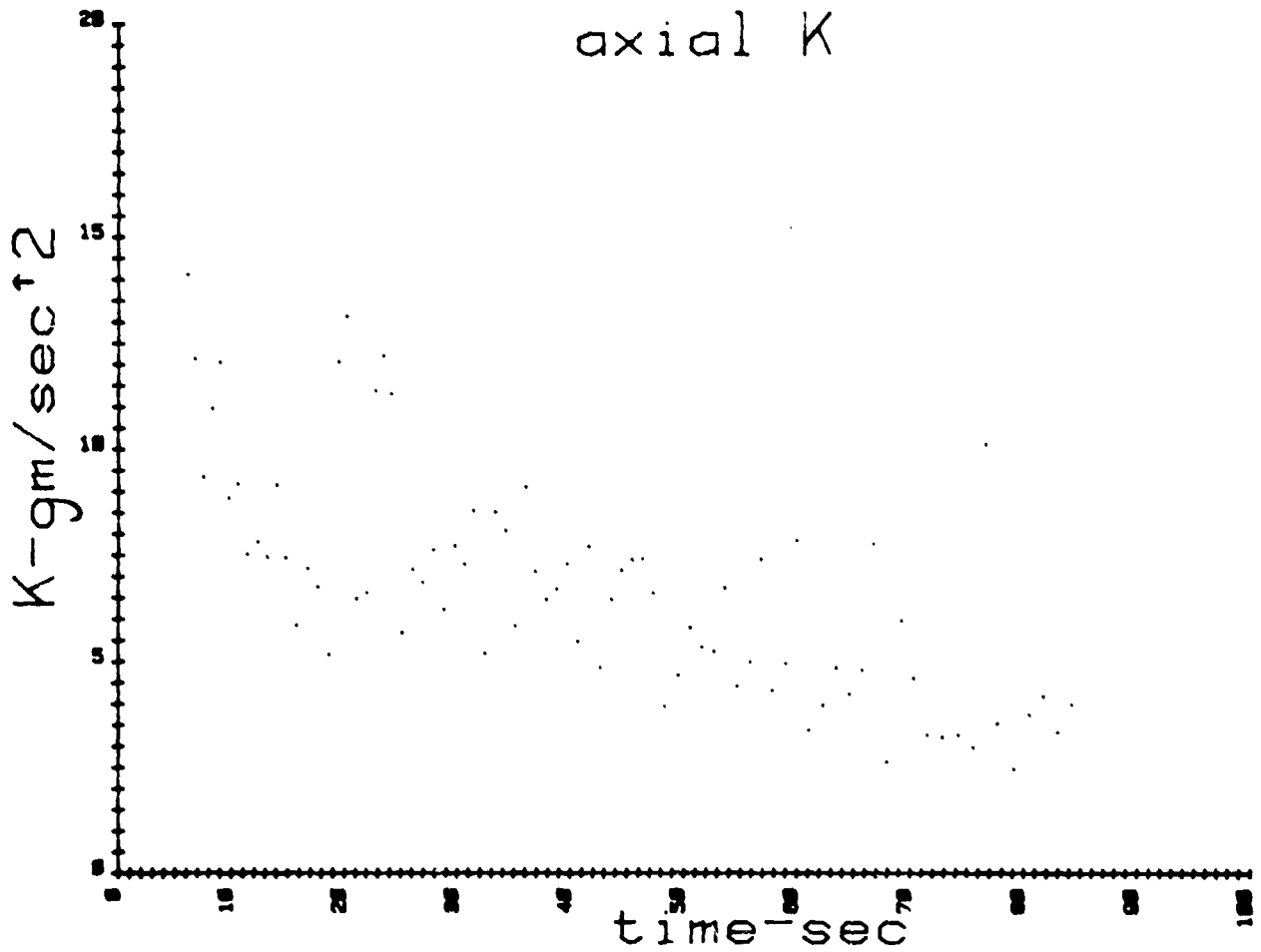


Figure 24. Axial force constant variation (harmonic oscillator model).

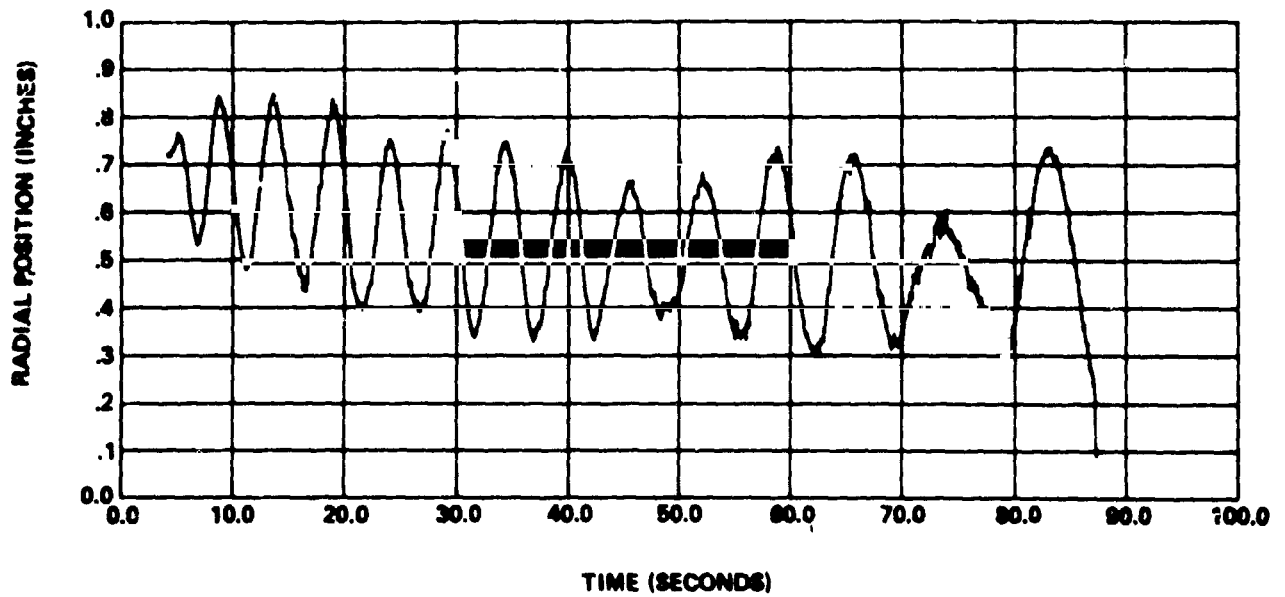


Figure 25. Radial motion of sample center.

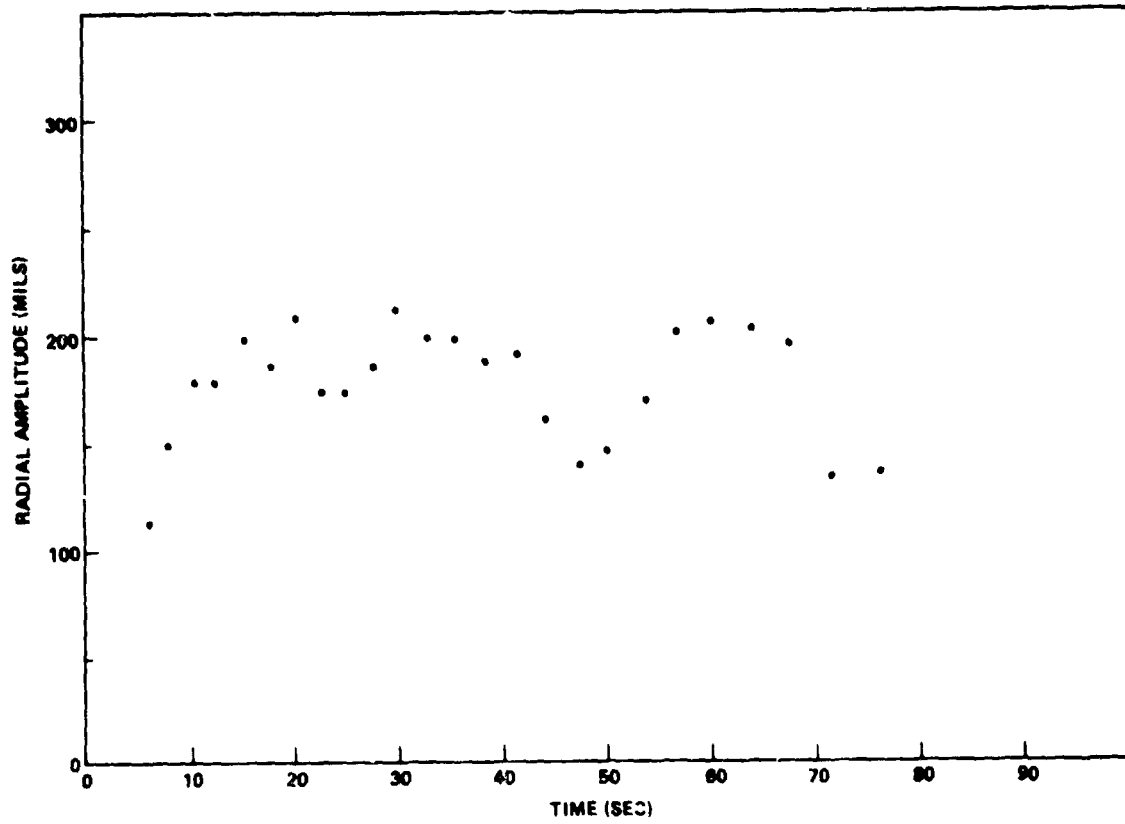


Figure 26. Radial amplitude variation.

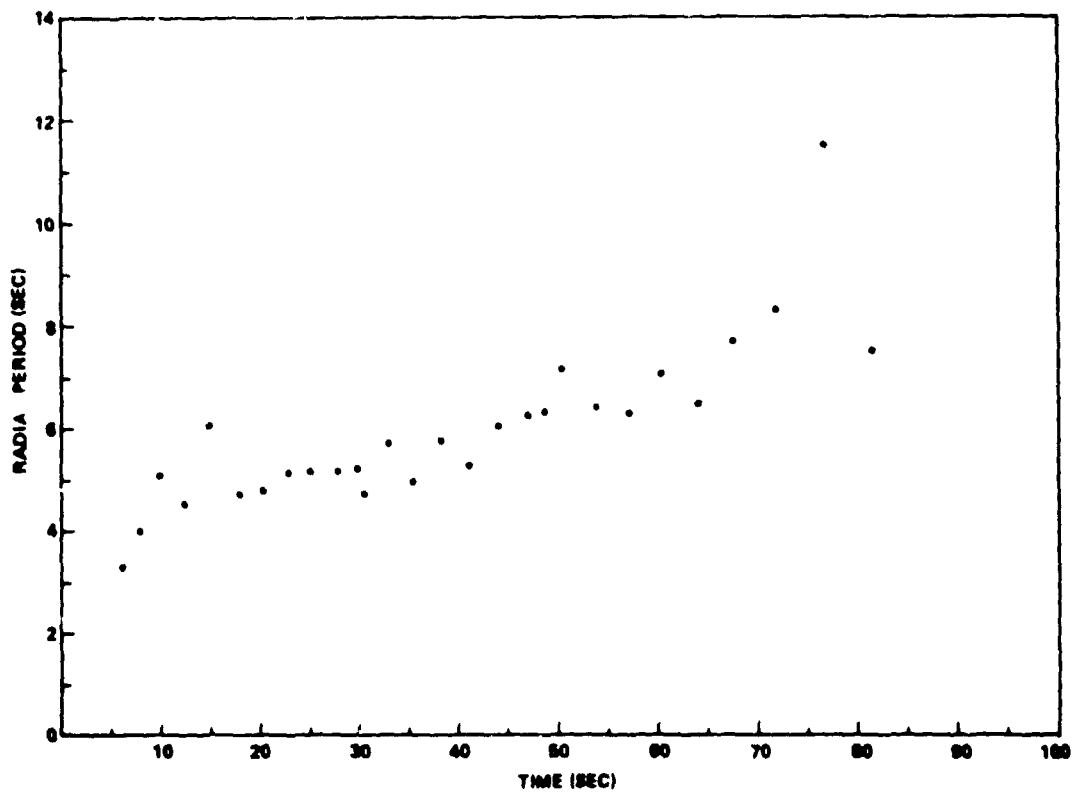


Figure 27. Radial period variation.

Figure 27 shows the time behavior of the period of radial oscillation. "Center of motion" drift, or average radial position as a function of time, is shown in Figure 28.

The $1/2k_r r^2$ potential approximation of the radial motion allows calculation of a force constant from the oscillation frequency. It is computed as in the axial case and is shown plotted as a function of time in Figure 29.

4. Sample trajectory in the y-z plane.

Appendix B consists of a sequence of plots of sample trajectory projected to the y-z plane (camera film plane). Plots are shown in their correct time sequence, with each plot representing 100 film frames or approximately 4.17 sec.

III. OBSERVED PHENOMENA REQUIRING EXPLANATION

The data presented previously comprise the complete set of raw data from the flight experiment and a set of secondary data based on sample position as a function of time. An aim of this work is to explain the phenomena observed in the data as completely as possible. Key phenomena are the following:

- 1) Oscillatory motion of the sample
 - a) axial component of oscillation
 - b) radial component of oscillation
- 2) Rotation of sample
 - a) Buildup of rotation about internal axis
 - b) orientation of rotational axis
 - c) magnitude of observed rotation rate
- 3) Variations in oscillation frequency
 - a) axial variations
 - b) radial variations
- 4) Variations in oscillation amplitude
 - a) axial variations
 - b) radial variations
- 5) Drift in average sample position
 - a) axial drift
 - b) radial drift

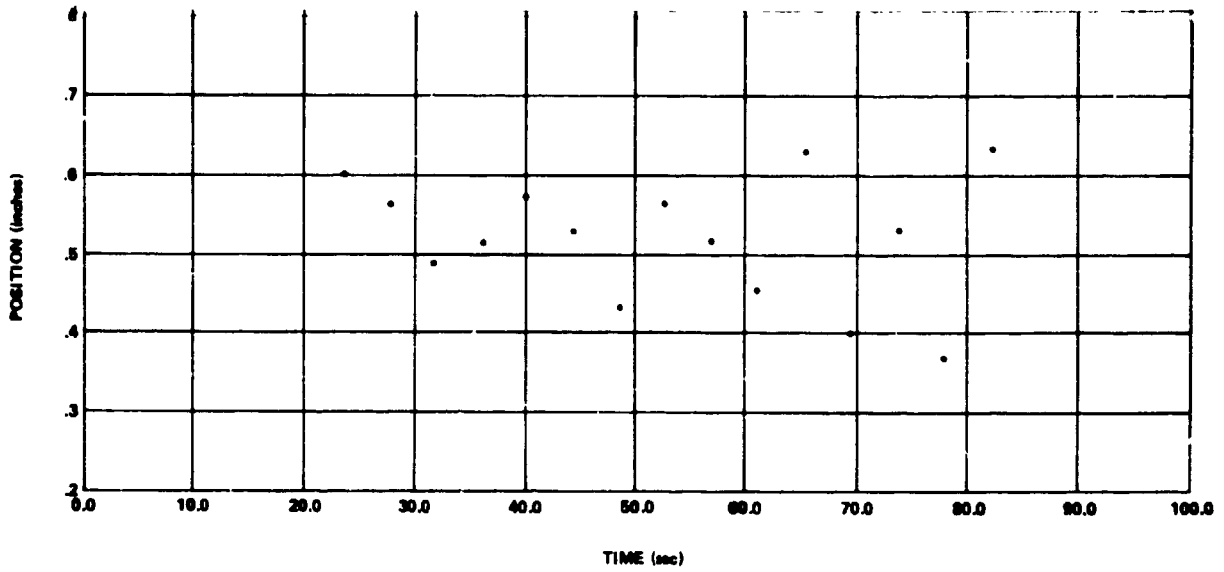


Figure 28. Radial position (100 frame averages).

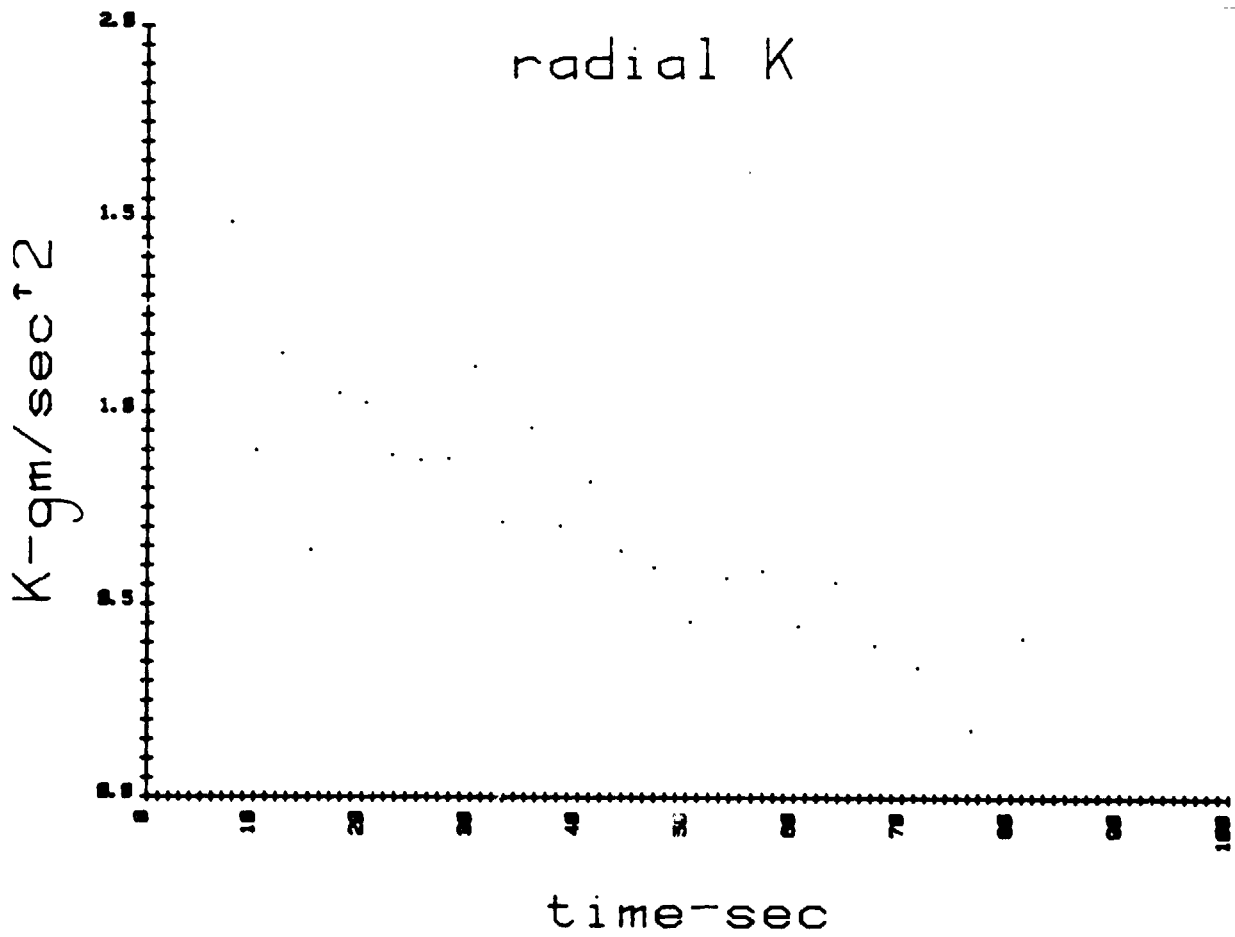


Figure 29. Radial force constant variation (harmonic oscillator model).

6) Sudden motion of sample followed by the sample coming to rest and remaining at rest for the duration of the experiment.

IV. FORCES ACTING ON SAMPLE

Before analyzing sample motion in detail, it is useful to catalogue the forces which can act on the sample. These are:

1) Forces due to the payload and its motion were measured by the low-g accelerometers and are derived from the rate gyro data. Measurements indicated that none of these is larger than a few times 10^{-5} g.

a) Drag from the interaction of the payload with the very tenuous atmosphere encountered during the low-g trajectory phase of the flight would be expected to be less than 10^{-7} g.

b) Impulses due to other experiments or from the payload assembly (e.g., gas venting) were not expected to be a problem, and the accelerometer data yield upper limits for these effects.

c) Centrifugal accelerations at the experiment location due to payload rotations were shown to be a few times 10^{-6} g or less.

d) Poincare forces ($\dot{\omega} \times \bar{r}$) due to angular accelerations were shown to be also of the level of a few times 10^{-6} g or less.

2) The sound field produced by the acoustic driver and reflector has a dc component which produces the positioning (or levitating) force. This will be discussed in further detail in Section V. This dc field is affected by several factors.

a) The density of the medium is related to the magnitude of the levitating force. This implies a temperature dependence. That is, as air temperature goes up (and density goes down), the levitating force decreases.

b) Geometrical effects in the acoustic system can be very important. For example, unwanted reflections can produce distortions in the axial symmetry of the dc sound field. These reflections can be produced by objects such as the sample injection assembly which intrude into the sound field.

c) Changes in moisture content of the levitating medium can result in sound absorption which can reduce pressure levels.

3) Acoustic streaming is also discussed in Section V. This flow produces aerodynamic forces on the sample. These forces may be important when the sample moves very near the cage assembly.

4) Aerodynamic forces due to sample motion (drag and magnus effect) are discussed in Section V. These forces are too small to influence sample motion appreciably.

5) Surface tension forces become dominant when the molten sample contacts the cage assembly. This causes the final rapid motion (about 1 sample radius in a time less than 1/24 sec). See Appendix C for a discussion of this.

V. ANALYSIS OF MOTION OF SPHERE

A. The Pressure Field

The force on a sphere in a high-intensity, standing-wave acoustic field was first predicted by King [1] and has since been verified experimentally. (The existence of radiation pressure in a sound field was originally predicted by Rayleigh, and the theory was developed in a series of 28 papers from 1902 to 1905.) The effect is one of second order in the fluid equations for the pressure in the sound wave.

The basic equations are

$$\frac{\partial \underline{u}}{\partial t} + (\underline{u} \cdot \nabla) \underline{u} = \frac{1}{\rho} \nabla p$$

$$\frac{\partial \rho}{\partial t} + \nabla \cdot (\rho \underline{u}) = 0,$$

where the viscosity term has been omitted from the first equation. This is acceptable for determining the pressure-velocity relationship but not for predicting acoustic streaming (to be discussed later).

For an irrotational fluid, King defines the velocity potential by

$$\underline{u} = -\nabla \Phi$$

and gets, in the simplest approximation,

$$\nabla^2 \Phi = \frac{1}{c^2} \frac{\partial^2 \Phi}{\partial t^2},$$

where $c = \sqrt{dp/d\rho}$ is the speed of sound. Taking p to be the variation from ambient pressure p_0 , the result for p to second order in \underline{u}^2/c^2 is

$$p = \rho_0 \frac{\partial \Phi}{\partial t} + \frac{1}{2} \frac{\rho_0}{c^2} \left(\frac{\partial \Phi}{\partial t} \right)^2 - \frac{1}{2} \rho_0 \underline{u}^2,$$

where ρ_0 is the ambient density.

King ignored any space dependence of ϕ other than that along the axis of sound source and reflector. If we generalize King's result to include a radial dependence, using cylindrical coordinates with cylindrical symmetry, we have

$$\phi = A R(r) \cos kz \cos \omega t,$$

where A is constant. Since the standing waves in a St. Clair generator are not confined to a well-defined cavity, we cannot treat the system by standard boundary-value theory. We can, however, require that the function R(r) give a radial dependence of the force on the sphere that corresponds to that which is observed. (We have done laboratory work on the force on a stationary sphere suspended from a microbalance, which can be combined with the work of Oran, et al. [2], to give a coherent picture.)

Taking

$$\phi \equiv \phi(r, z) \cos \omega t$$

we get

$$\frac{d^2 R}{dr^2} + \frac{1}{r} \frac{dR}{dr} + \gamma^2 R = 0,$$

where $\gamma^2 = \frac{\omega^2}{c^2} - k^2$. (Note that if there is radial dependence in ϕ , $k \neq \omega/c$.)

Such an effect ($k \neq \omega/c$) is apparent in data already available from Oran, et al. [2]. They measured the axial force in a sphere at room temperature and got force maxima at a separation of 1.41 cm, corresponding to a k value of 2.22 cm^{-1} , compared to the value of ω/c (at 15 kHz) of 2.73 cm^{-1} , and giving $\gamma = 1.59 \text{ cm}^{-1}$.

The radial equation given previously has a solution

$$R(r) = J_0(\gamma r),$$

where J_0 is the zeroth order Bessel function and γ is to be determined experimentally. Using this result in the pressure equation, we get

$$p = -\rho_0 \omega A J_0(\gamma r) \cos kz \sin \omega t + \frac{1}{2} \frac{\rho_0}{c^2} \omega^2 A^2 J_0^2(\gamma r) \cos^2 kz \sin^2 \omega t \\ - \frac{1}{2} \rho_0 A^2 \left[\gamma^2 J_1^2(\gamma r) \cos^2 kz + k^2 J_0^2(\gamma r) \sin^2 kz \right] \cos^2 \omega t,$$

with $\frac{dJ_0}{dr} = -\gamma J_1(\gamma r)$. We get the "dc" pressure by averaging over one or more cycles:

$$\bar{p} = \frac{1}{4} \rho_0 \gamma^2 A^2 \left[J_0^2(\gamma r) - J_1^2(\gamma r) \right] \cos^2 kz + \frac{1}{4} \rho_0 k^2 A^2 J_0^2(\gamma r) \cos 2 kz.$$

The last term, with $J_0 \rightarrow 1$, is the result obtained by King, valid for $\gamma r \ll 1$.

If we take the force on the sphere to be given by

$$\underline{F} \approx -(\text{const}) \nabla \bar{p},$$

we can compare the radial and axial parts. This is equivalent to defining a potential-energy function $V(r, z)$ with $V(r, z) \propto \bar{p}$ and taking

$$V(r, z) = V_0 + \frac{1}{2} k_z z^2 + k_r r^2 + \dots$$

We find k_z/k_r at the equilibrium point (near $r = 0$, $z = \pi/2k$) to be given by

$$k_z = 2K (2k^2 + \gamma^2) k^2$$

$$k_r = K \gamma^2 k^2$$

$$k_z/k_r = 2(2k^2 + \gamma^2)/\gamma^2.$$

If we determine the periods of small radial oscillations, we have

$$k_z/k_r = T_r^2/T_z^2, \quad \text{giving} \quad \frac{1}{2} \frac{T_r^2}{T_z^2} - 1 - \gamma^2 = 2 k^2$$

and, of course, $k^2 + \gamma^2 = \omega^2/c^2$. Taking the data from SPAR VIII, we get $T_r/T_z \approx 3$. This gives

$$k = \sqrt{7 \gamma/2}.$$

With $\omega/c = 1.09 \text{ cm}^{-1}$ at 1575°C , we get

$$k = 0.87 \text{ cm}^{-1}, \quad \gamma = 0.66 \text{ cm}^{-1}.$$

We can use these values to estimate the departure of the potential energy function from Hooke's law. There is obviously more to be done in the study of the pressure function, including a reconciliation of King's result $F_z = -\frac{5}{4} V \bar{dp}/dz$. Plots of the force and potential from the preceding calculations are given in Figures 30 through 33.

B. Orbit of the Sphere

Consider the radial motion of the sphere. Since k_r and k_z are essentially constant, we can treat the axial motion and the motion in the radial plane as independent. We approximate $V(r)$ by

$$V(r) = \frac{1}{2} k_r r^2.$$

With the substitutions

$$u = 1/r \qquad u \equiv \frac{du}{dt} = \frac{du}{d\theta} \theta$$

the equation for the orbit becomes [3]

$$\theta - \theta_0 = - \int_{u_0}^u \frac{du}{\sqrt{\frac{2mE}{\ell^2} - \frac{2mV}{\ell^2} - u^2}}.$$

The substitution $x = u^2$ gives an integral of the form

$$I = \int_{x_0}^x \frac{du}{\sqrt{a + bx + cx^2}}$$

with the result

$$\frac{1}{r^2} = \frac{1}{r_0^2} - \frac{1}{2} \sqrt{A^2 - 4B} \sin \left[2(\theta - \theta_0) \right],$$

where $A = \frac{2mE}{\ell^2}$, $B = \frac{mk_r}{\ell^2}$.

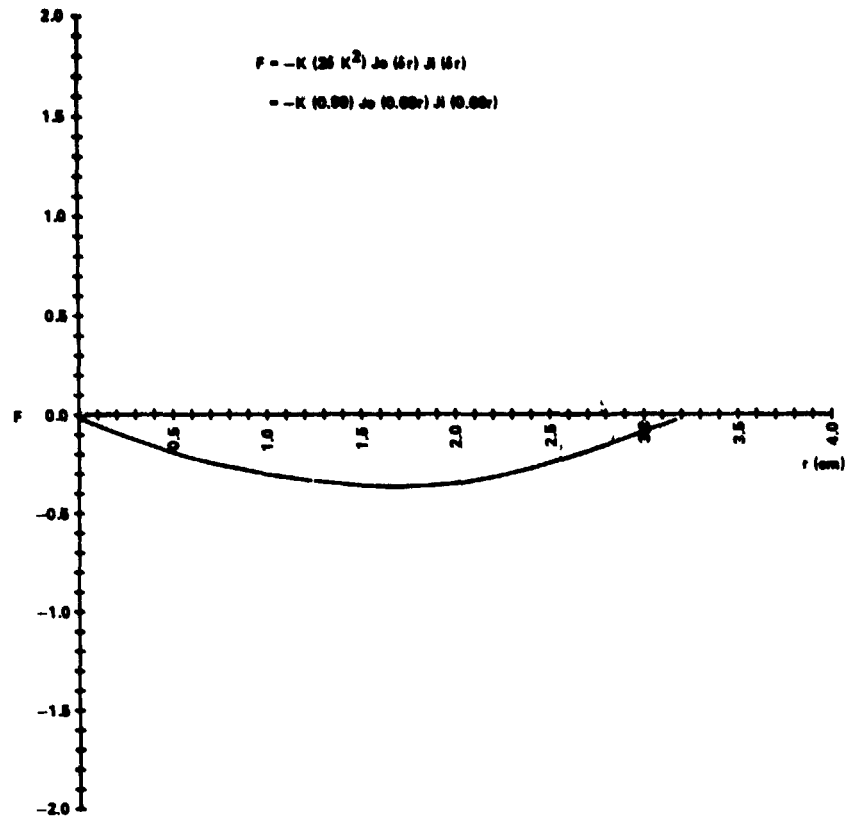


Figure 30. Radial dependence of force in equilibrium plane.

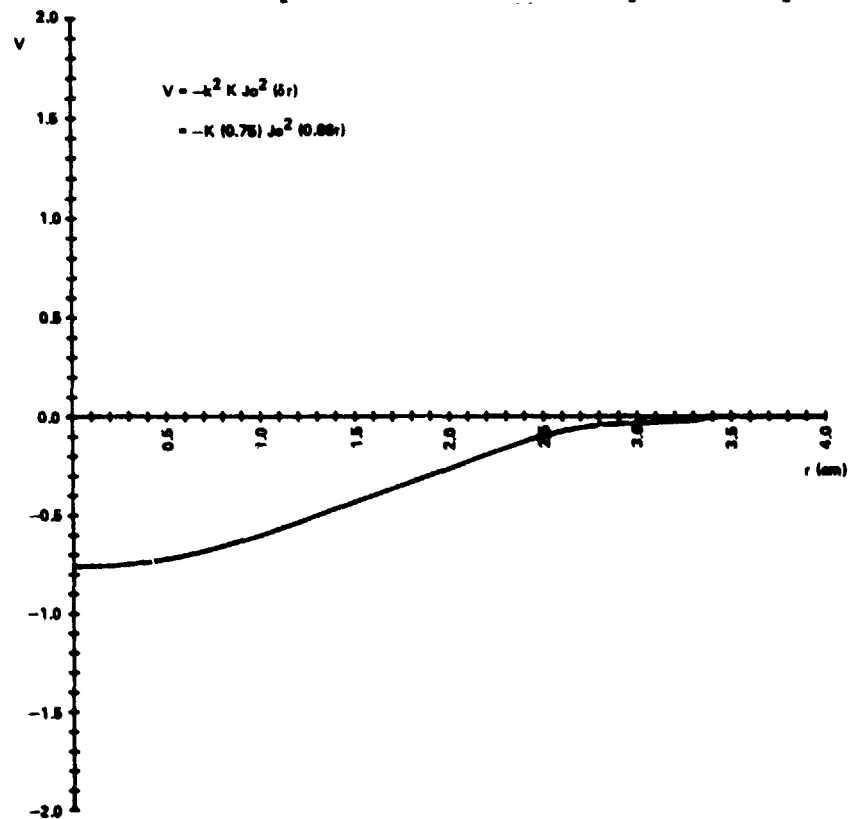


Figure 31. Radial dependence of potential energy function in equilibrium plane.

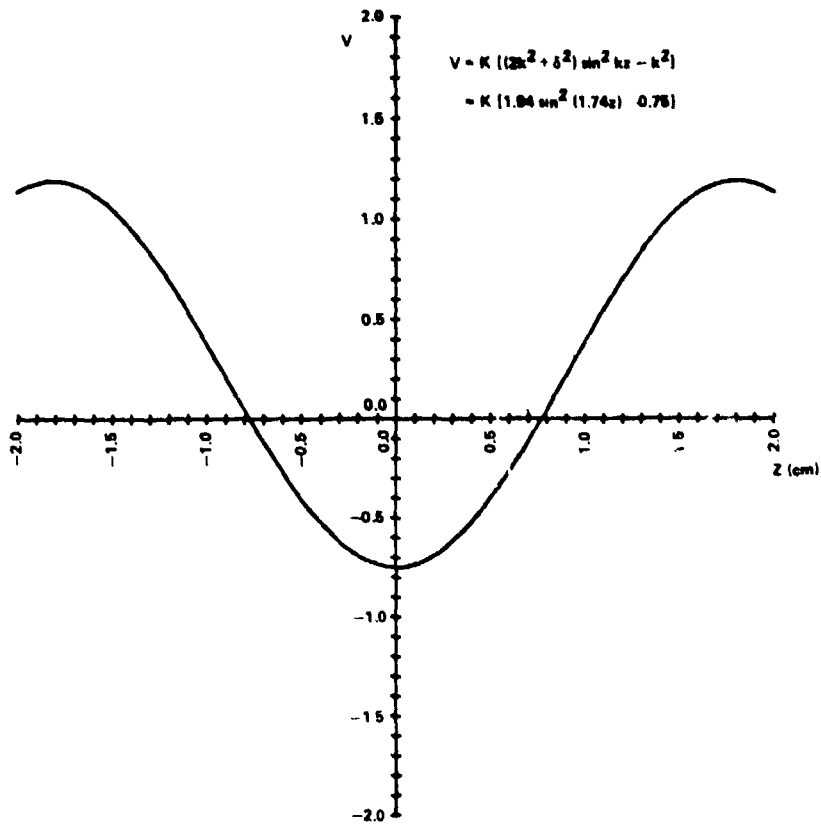


Figure 32. Axial dependence of potential - energy function.

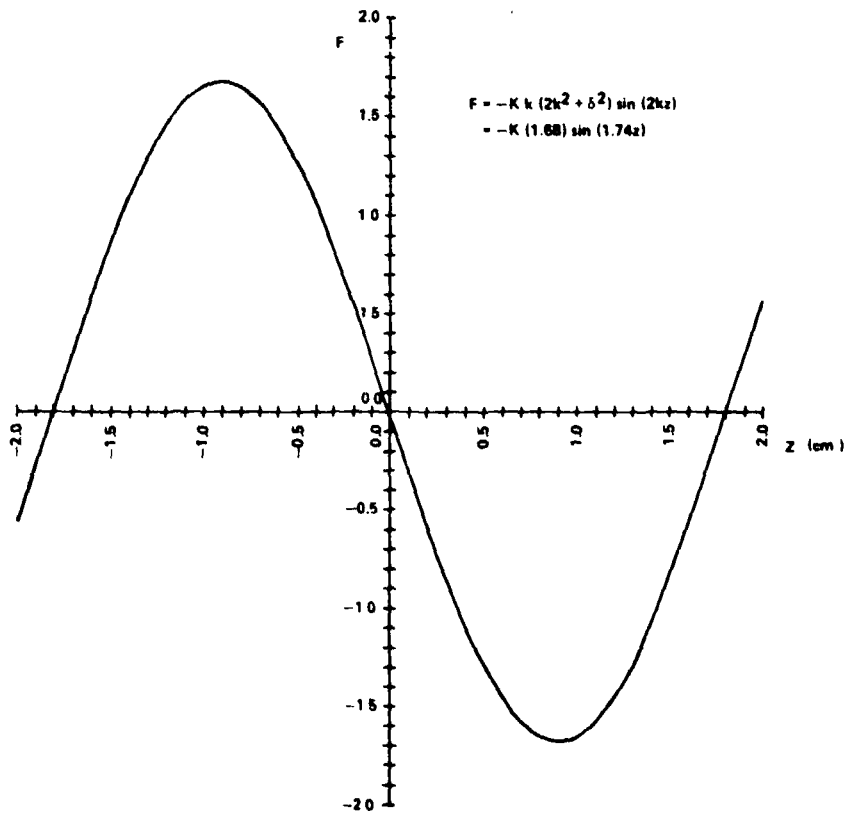


Figure 33. Axial dependence of force.

The energy equation is [1]

$$E = \frac{1}{2} m r'^2 + \frac{\ell^2}{2mr^2} + \frac{1}{2} k_r r^2,$$

and so the turning points of the radial motion given by [4]

$$E = \frac{\ell^2}{2mr_{1,2}^2} + \frac{1}{2} k_r r_{1,2}^2 \quad \text{or} \quad \frac{\ell}{r_{1,2}^2} = \frac{A}{2} \pm \frac{1}{2} \sqrt{A^2 - 4B}.$$

The simplest form is obtained by choosing $\theta_0 = \pi/4$, so that

$$\frac{1}{r^2} = \frac{A}{2} + \frac{1}{2} \sqrt{A^2 - 4B} (\cos^2 \theta - \sin^2 \theta),$$

which is easily shown to be an ellipse with the center at the origin, major axis along the x axis, and semi-major and semi-minor axes r_1 and r_2 given by

$$\frac{1}{r_1} = \frac{1}{2} A - \frac{1}{2} \sqrt{A^2 - 4B} \quad \frac{1}{r_2} = \frac{1}{2} A + \frac{1}{2} \sqrt{A^2 - 4B}.$$

The period τ of the motion follows from Kepler's second law [2]:

$$\tau = \frac{2m}{\ell} S,$$

where S is the area of the ellipse. We find

$$\omega_r \equiv \frac{2\pi}{\tau} = \sqrt{\frac{k_r}{m}}.$$

The idealized motion of the sphere (no perturbations, no departure from Hooke's law force) is thus an elliptical orbit with angular velocity ω_r modified by axial oscillations with angular frequency $\omega_r = \sqrt{k_z/m}$.

The problem is also separable in Cartesian coordinates, and we get for the time dependences of the motion,

$$x = A_1 \cos (\omega_r t + \phi_1)$$

$$y = A_2 \cos (\omega_r t + \phi_2)$$

$$z = A_3 \cos (\omega_z t + \phi_3).$$

If the ellipse is oriented as given previously, the x and y equations are

$$x = r_1 \cos \omega t$$

$$y = r_2 \sin \omega t.$$

C. Perturbations of the Orbit

1. Time independent corrections to Hooke's law.

Bertrand proved [3] that the only central forces that give exactly closed orbits are the inverse-square force and the Hooke's law force. Thus, any modification to the potential in Part B will give an orbit that is not closed. The time-independent modification takes the form of a fourth-power term in the expansion of the radial potential. For approximately circular orbits the effect of such a correction can be estimated. The correction to $u \equiv \frac{1}{r}$ is given by [3]

$$u = u_0 + a \cos \beta \theta,$$

where $\beta = 2$ for a Hooke's law force. One can then show [4] that

$$\beta^2 = 3 + \frac{r}{F_r} \left. \frac{dF_r}{dr} \right|_{r=r_0},$$

where r_0 is the average value of r and F_r is the radial force.

From the expansion

$$\begin{aligned} J_0^2(x) &= 1 - \frac{1}{2} x^2 + \frac{3}{16} x^4 - \dots \\ &= 1 - \frac{1}{2} \gamma^2 r^2 + \frac{3}{16} \gamma^4 r^4 - \dots \end{aligned}$$

and the definition of a fourth-power coefficient,

$$V(r) = V_0 + k_r \left(\frac{1}{2} r^2 - \frac{1}{4} br^4 + \dots \right),$$

we see that $b = \frac{3}{4} \gamma^2$, and

$$\frac{r}{F_r} \frac{dF_r}{dr} = 1 - 2br^2 + \dots$$

This gives

$$\beta^2 = 4 - 2br_0^2 = 4 - \frac{3}{2} \gamma^2 r_0^2$$

or

$$|\Delta \beta| = 2 - \beta \lesssim 0.04$$

for $\gamma = 0.66 \text{ cm}^{-1}$ and $r_0 \approx r_{\text{max}}$.

The significance of this result is that the correction term causes the elliptical orbit to precess in the angular direction of the orbit. Qualitatively, this occurs because angular momentum is conserved; but the sphere stays near r_{max} longer than it would for a pure Hooke's law force. The amount of precession, measured in the fraction of one complete cycle of precession for one cycle of the elliptical motion, is $\nabla\beta$. That is, after one cycle of θ in a space-fixed reference frame, the sphere has not quite returned to its original radial position. Our estimate shows that the precession could be up to $\sim 200^\circ$ in 14 cycles, or slightly more than $\frac{1}{2}$ of a revolution. During the total motion of the sphere, the amplitude could thus go from a minimum to a maximum and back, or vice versa.

2. Time-dependent force constant.

The data on the position of the sphere indicate a time variation of the force constants k_z and k_r in such a way that $k_z/k_r \approx \text{constant}$. This indicates a decrease in the dc pressure in the sound field, the explanation for which is discussed elsewhere. We consider here the effect of this time-dependence of k_z and k_r on the motion.

The equations of motion retain their same form and are modified only by the fact that the force constants are time dependent:

$$m\ddot{r} - \frac{\ell^2}{mr^3} = -k_r(t) r$$

$$m\ddot{z} = -k_z(t)z$$

with ℓ , the angular momentum in the plane of the orbit, still constant.

Starting at $t = 5 \text{ sec} \equiv t_0$, we find from the data that $k_z(t)$ makes an abrupt change of about 50 percent during the first 5 sec and a gradual change of about 40 percent during the next 60 sec, after which the motion becomes quite erratic. Let us consider the middle portion during which the change is relatively slow.

If $k_z(t)$ changes sufficiently slowly, we can represent the motion by

$$A(t) = A_3(t) \cos [\omega(t) t + \phi(t)]$$

(adiabatic approximation). This approximation will be good if $\Delta\omega/\omega \ll 1$ for one cycle, a condition which holds reasonably well during the period from $t = 10 \text{ sec}$ to $t = 70 \text{ sec}$. Einstein proved [3] that in the adiabatic approximation the ratio of the mean energy to the frequency remains constant. The problem was earlier solved by Rayleigh as the starting point of his study of radiation pressure (1902).

Einstein's result also follows from the Boltzmann-Ehrenfest theory of adiabatic invariance (1913). The energy in this approximation is (considering the axial motion only)

$$E_z = \frac{1}{2} m \omega^2 A_3^2,$$

so we get $\omega A_3^2 = \text{const}$ or $A_3 \propto \frac{1}{\sqrt{\omega}}$. The change in ω is from $\omega_1 \approx 3.5/\text{sec}$ to $\omega_2 \approx 2.6/\text{sec}$. This gives about a 20 percent increase in A_3 . The actual behavior of A_3 is quite different from this, indicating that some other perturbations are dominating the amplitude but not significantly affecting the period.

3. Numerical analysis.

The preceding analysis indicates that the potential function describing sample motion in the acoustic levitation system is time dependent and requires terms in the radial equation higher than second order. For the radial potential function we use the form:

$$V(r,t) = K_0 \left(\frac{1}{1+Bt} \right)^2 (r^2 + Ar^4).$$

From the flight data K_0 is determined to be approximately 1.5 in cgs units. B is estimated from the time behavior of the period to be approximately $8.6 \times 10^{-3} \text{ sec}^{-1}$. A is obtained by applying the solution of the time-independent correction (discussed in Section V.C.1) to the geometry of the flight acoustic levitator. A is estimated to have the value of -0.33 cm^{-2} . Other parameters are the sample mass (0.6 gm) and an estimate of initial orbital angular momentum of the sample ($\leq 0.2 \text{ gm cm sec}^{-1}$). The estimate of angular momentum comes from assumption of near-circular orbit and measurements of sample mass and orbital period.

The force derived from the preceding radial potential function is:

$$F(r,t) = -K_0 \left(\frac{1}{1+Bt} \right)^2 (2r + 4Ar^3).$$

The equation

$$m\ddot{r} - \frac{L^2}{mr^3} = -K_0 \left(\frac{1}{1+Bt} \right)^2 (2r + 4Ar^3)$$

was solved numerically, using the parameters shown previously, to yield a sample orbit. Figure 34 shows the first $2\frac{1}{4}$ cycles of the computed orbit. The important qualitative feature that can be seen here is that an orbit approximating a precessing ellipse has been obtained. The integration has been carried out for 90 sec, and a projection of the resulting orbit onto a line in the orbital plane is shown in Figure 35.

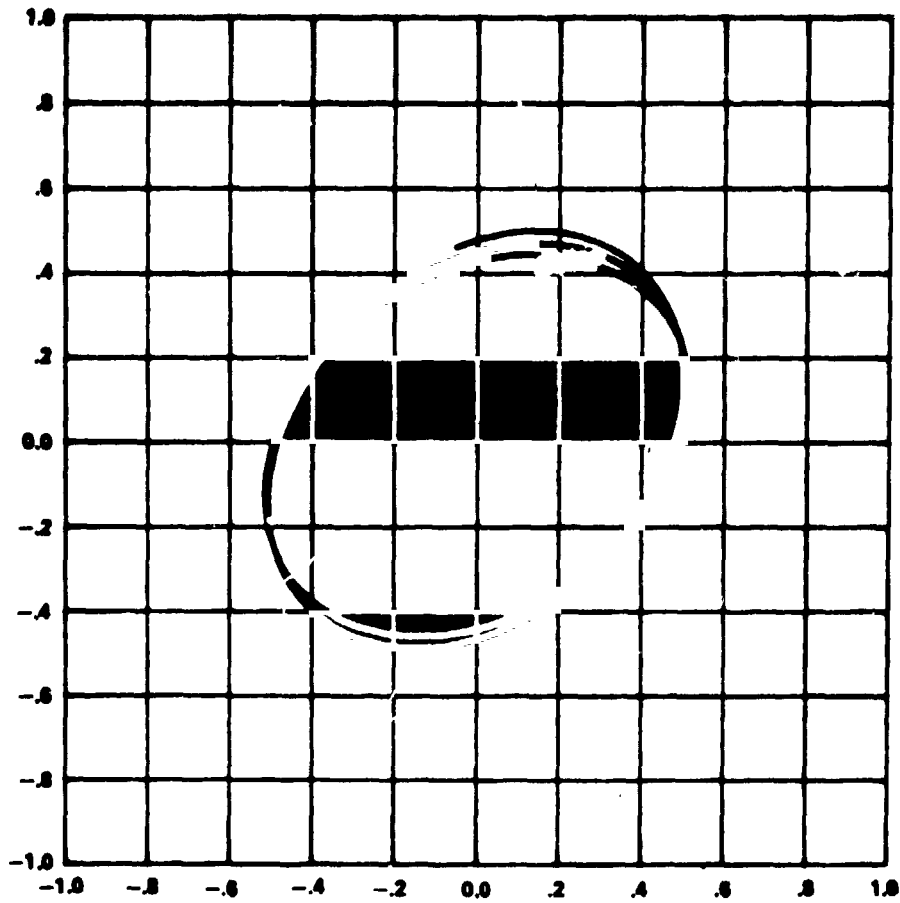


Figure 34. Calculated sample orbit.

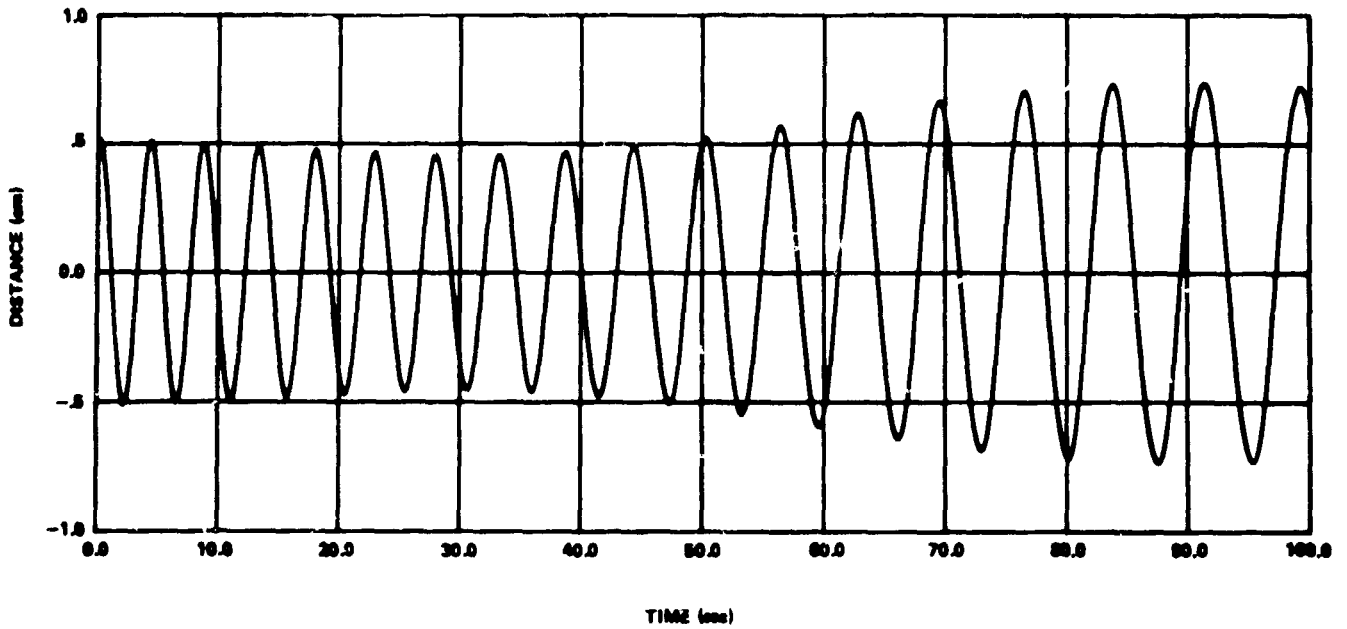


Figure 35. Projection of calculated orbit onto a line.

This projection of the orbit reveals some features seen in the flight data. First, there is a secular amplitude variation reminiscent of the variation seen in the flight data (Figure 26). This is the result of observing the orbit from the orbital plane and seeing projections of the orbit which vary as the orbit precesses. We also see an increase in the orbital period with time, as is noted in the flight data (see Figure 27). Figure 36 is another projection of the radial component of motion with the same input parameters as previously, except that $A = -0.5 \text{ cm}^{-2}$. The result is qualitatively the same as before, but the increase in the orbital period is faster than before. The change in A represents a shallower potential well, as indicated in Figure 2.

If $A = 0$ (that is, the potential is restricted to an r^2 dependence in its spatial variation), the first few cycles of the resulting sample orbit will be as shown by Figure 37. We see that the precession of the orbit is now very slight. The fairly rapid precession implied by the radial amplitude variations then dictates the need for spatial variations of higher than second order.

4. Drag.

There will be drag forces on the sphere because of its motion relative to the air, which itself also has a time-independent flow known as acoustic streaming. The force is usually represented by the equation

$$F_D = \frac{1}{2} \rho_0 A v^2 C_D$$

$$= (3.02 \times 10^{-5}) v^2 C_D \text{ (cgs units),}$$

where F_D is the drag force, A is the cross-sectional area of the sphere, v is the speed of the sphere relative to the air, and C_D is the drag coefficient [5]. The drag coefficient depends only on the Reynolds number R (for uniform flow without boundaries), defined by

$$R = \frac{Dv}{\nu},$$

where D is the diameter of the sphere, ν is the kinematic viscosity, and $\nu \equiv \mu/\rho_0$ where μ is the (dynamic) viscosity. For our sphere at 1575°

$$R = 0.204 v$$

for v in cm/sec. C_D has been determined for a broad range of values of R and is plotted, e.g., in Reference 5.

We first estimate the drag force which would exist in still air due to motion of the sphere. A typical maximum speed is obtained from the amplitude and

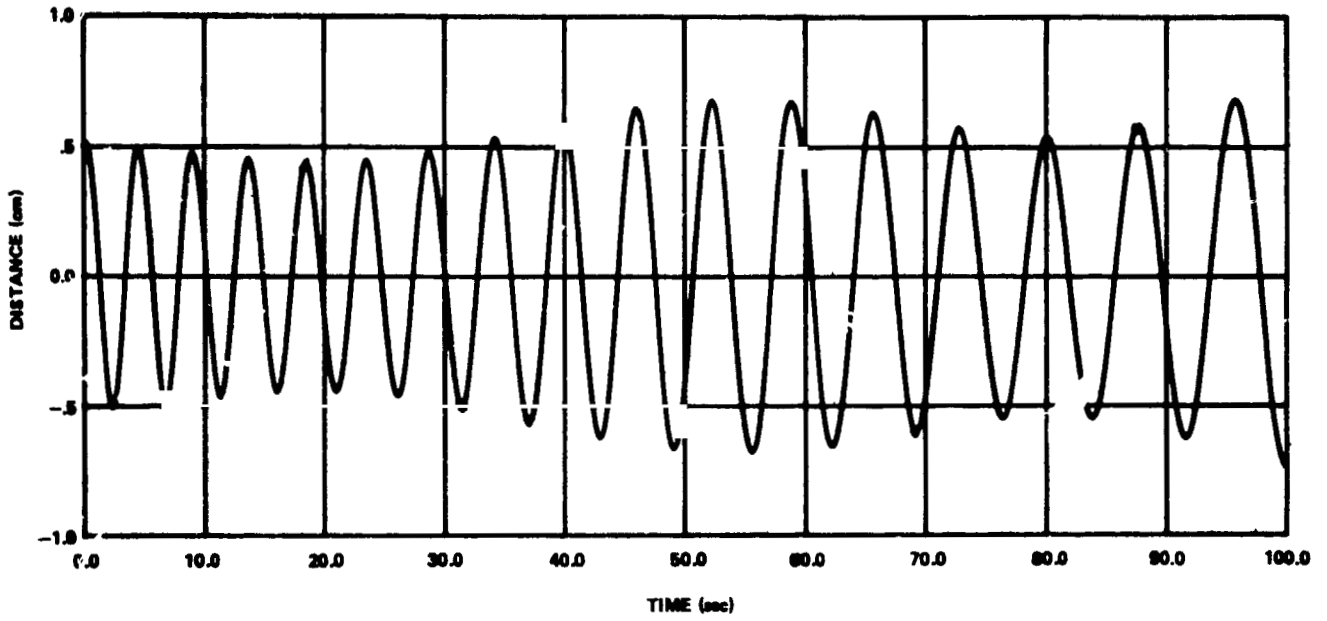


Figure 36. Projection of calculated orbit onto a line.

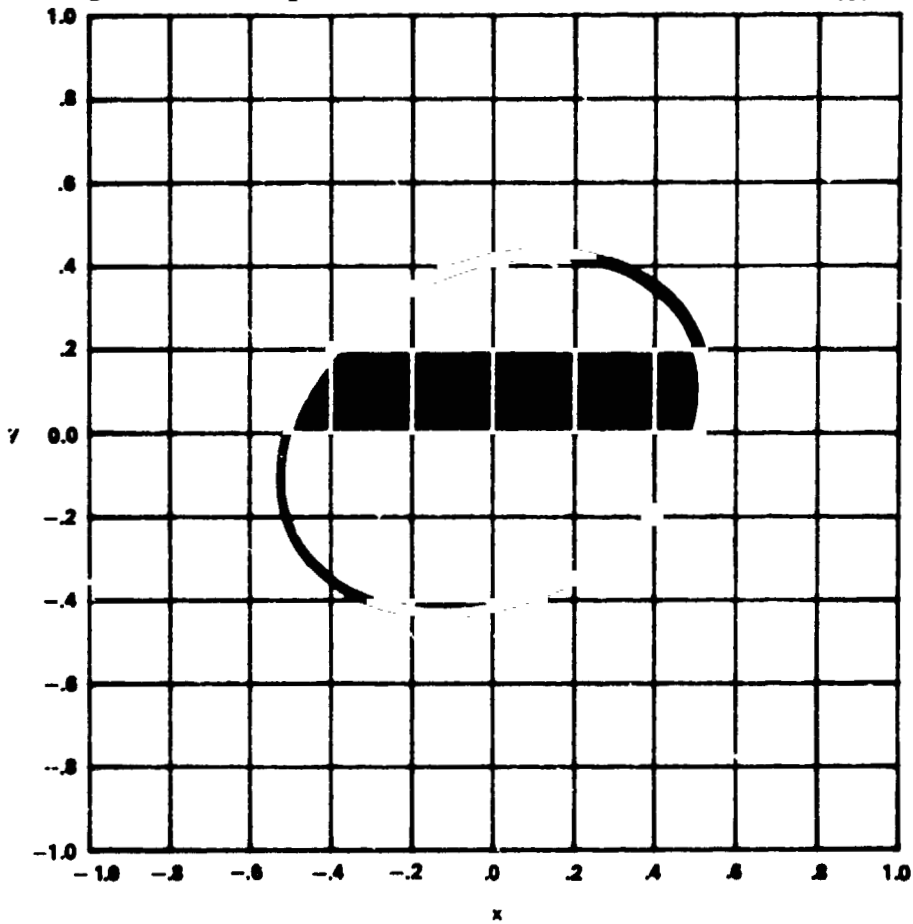


Figure 37. Sample orbit.

frequency data. Taking radial and axial amplitudes of 0.5 cm and 0.25 cm and angular frequencies of 1.5/sec and 5/sec, respectively, as near maximum values, we get a maximum speed of 1.5 cm/sec. (We will see later that acoustic streaming numbers are larger.) This gives $R \approx 0.3$, $C_D \approx 100$ and $F_O \approx 5 \times 10^{-3}$ dynes. Typical values during the motion will be much smaller. (Stokes' law gives $F_O = 3.6 \times 10^{-3} v$.)

Thus it appears that we can ignore the motion of the sphere itself and consider only acoustic streaming when estimating drag effects.

5. Spin.

Since the sphere was determined to be spinning during part, if not most of the motion, we should also consider the force on it due to its spin (Magnus effect; see Reference 5, p. 71). The force per unit length F_t/ℓ on a rotating cylinder moving at speed v is given by [5]

$$F_t/\ell = \rho \Gamma v,$$

where Γ is the circulation of the cylinder [5]. We can calculate the equivalent effect on a sphere as

$$\begin{aligned} F_t &= \frac{8}{3} \pi \rho_0 v a^3 \omega_s \\ &= 5.12 \times 10^{-5} v \omega_s \text{ (cgs units),} \end{aligned}$$

where a is the radius of the sphere and ω_s is spin angular velocity. For motion due to the sphere alone, using $v = 1.5$ cm/sec as before and an estimated value for ω_s based on a (guessed) rotational frequency of 10 Hz, we get

$$F_t \approx 3 \times 10^{-4} \text{ dynes.}$$

Thus we could increase ω_s by two orders of magnitude and still ignore F_t . We will reconsider spin, however, in connection with acoustic streaming.

6. Acoustic streaming.

High-intensity sound waves in air are accompanied by time-independent (dc) flows known as acoustic streaming (see, e.g., Reference 6 and 7). These flows occur in a free nonuniform sound field, near objects in the field, and near oscillating bodies. They are intimately related to the subject of radiation pressure which gives the force used for positioning of the sphere. They were first noted by Faraday (1831) and were studied by Rayleigh in connection with radiation pressure [8].

For streaming around an object in a sound field, there is a dc boundary layer which separates two flows. The inner flow is known as Schlichting streaming and the

outer one as Rayleigh streaming. Flow in a free nonuniform sound field is known as Eckart streaming. For all three types, stability is governed by viscous forces.

The nature of streaming in a standing wave field is known qualitatively and quantitatively at low intensities, and some work has been done at high intensities. An estimate of the magnitude of the dc velocity can be obtained from the measurements of Borisov and Statnikov [9] at high intensities. They used three different methods to measure the axial component of the dc flow velocity in a circular tube and reported the maximum values versus dc pressure, giving

$$\bar{u} \sim b \bar{p}^2,$$

with $b = 2.2 \times 10^{-3} (\text{cm/sec}) / (\text{dyne/cm}^2)^2$. The curve was determined for sound pressure levels between 163 and 168 db, with measurements at lower SPL giving values smaller than those predicted by the curve.

The basic relationships are:

sound pressure level:

$$\text{SPL} = 20 \log_{10} (P_{\text{rms}}/p_s),$$

where P_{rms} is the root-mean-square pressure in the sound wave and p_s is the standard reference pressure $p_s = 2 \times 10^{-4} \text{ dyne/cm}^2$.

dc pressure:

$$\bar{p} \sim P_{\text{rms}}^2 / 2\rho_0 c^2,$$

where $\rho_0 c^2 = \gamma P_0$ for ideal gas, with $\gamma =$ ratio of heat capacities of air and $P_0 =$ mean reference pressure = mean pressure in payload. Thus,

$$\bar{u} \propto P_{\text{rms}}^4.$$

according to Borisov and Statnikov. For a sample density ρ_1 of 4.43 gm/cm^3 we can calculate the approximate value of P_{rms} using an equation given by King [1]. King's result gives

$$P_{\text{rms}} = \sqrt{\frac{2}{5} \rho_0 \rho_1 \frac{c}{k} n},$$

where n is the angular frequency of axial oscillations of a sphere in the sound field.

We have checked the relation of u to \bar{p} given by Borisov and Statnikov in the laboratory at room temperature by photographing spheres of uniform density ($50 \mu\text{m}$) in the sound field at measured intensity, using a well-defined laser beam for

illumination. The results agree reasonably well. For a determination of \bar{u} at 1575°C, however, we must also take account of the variation of kinematic viscosity with temperature. Reynolds' principle of similarity (see, e.g., Reference 5) gives $\bar{u} \propto \nu$. For the same value of P_{rms} , then, the expected value of \bar{u} will be greater by the ratio of kinematic viscosities:

$$\nu'/\nu = 3.12/0.15 = 21.$$

The results, using the formulae of King and of Borisov and Statnikov with the preceding factor, give the values shown in Table 1. The values of n are the ω values quoted in Section V.C.2.

TABLE 1. ESTIMATED MAXIMUM VALUES OF ACOUSTIC STREAMING VELOCITY

$n(\text{sec}^{-1})$	$P_{rms}(\text{dyne/cm}^2)$	SPL(db)	$\bar{p}(\text{dyne/cm}^2)$	$\bar{u}(\text{cm/sec})$
3.5	6.4×10^3	150	14.7	10
2.6	4.8×10^3	148	8.1	3

From the discussion in Section V.C.3, we find that for $\bar{u} = 10$ cm/sec, $R = 2$; this is still within the range where Stokes' law holds (force \propto velocity), and we find that typical forces on the sphere due to acoustic streaming are less than $\sim 4 \times 10^{-2}$ dynes.

Although our data on acoustic streaming are not yet definitive, it appears that the highest streaming velocities occur at the greatest distances from the equilibrium position, within the range of motion of the sphere. This is, of course, also where the restoring force is greatest. By comparison, the restoring force is ~ 1 dyne. Thus, while streaming forces are not of the same order of magnitude, they are not negligible in determining the shape of the position versus time curves and appear to be of about the same relative importance in this respect (shape, rather than period) as the precession and the time variation of the force constants discussed previously.

It should be pointed out here that one cannot determine the streaming velocities from the equations in Section V.A., since they are produced by the stress term [7], $\mu \nabla^2 \underline{u}$, which was omitted from these equations in a calculation of the pressure.

Whether we could make accurate predictions of the shape of the position versus time curves by detailed studies of the streaming is relatively unlikely. However, we believe that a knowledge of the direction and magnitude of the streaming velocities in high-intensity sound fields will be important for implementation of acoustic levitation devices. Certainly streaming is primarily responsible for the shearing forces which cause samples to spin, and we know that the spin can be affected by adjusting the angle and/or the position of the reflector.

VI. SUMMARY AND CONCLUSIONS

A. Summary

In this report we have given a description of the single-axis acoustic levitation experiment on SPAR-VIII. We reviewed the primary data, mainly a film of the sample motion, and various graphical and digital representations of these data.

Having presented the data, we then identified the phenomena which, in our judgment, could or should be explained. This led to an analysis of the forces acting on the system, an estimate of their relative magnitudes based on a theoretical model, and a study of the effects of those forces which seem to be significant.

B. Conclusions

Here we list, briefly, the conclusions which we have drawn based on our analysis, as discussed in more detail in the body of the report.

- 1) There are no forces due to anything external to the experiment package itself which had any significant effect on the motion of the sample.
- 2) The shift in the axial equilibrium position was caused by the cooling of the air on injection of the sample and its subsequent return to operating temperature as the experiment progressed (see Appendix D).
- 3) The shift in the radial equilibrium position was due to a combination of an asymmetric distortion of the acoustic field caused by the injection device and the temperature change and axial shift discussed above (see Appendix D).
- 4) The gradual increase in the radial and axial periods (with constant ratio) was due to a lowering of the sound pressure level. This resulted from increased water vapor due to evaporation from the injector and sample as they heated up. Conclusions 2, 3, and 4 are drawn pending further experimental confirmation from Interasonics, Inc.
- 5) The gross features of the motion were what one would expect from the theoretical model which was presented. They consisted of an elliptical motion in the radial plane coupled with axial oscillations.
- 6) The modifications in the amplitude are due to a combination of effects. In the absence of three-dimensional data, these effects cannot be isolated. The primary ones are coupling between the radial and axial oscillations due to the nature of the pressure field, elliptical precession due to the fact that the radial potential is not purely simple harmonic, and drag due primarily to acoustic streaming.
- 7) The apparently random changes in shape of the position versus-time plots are due primarily to acoustic streaming. We draw this conclusion based on our estimated magnitude of the streaming velocity and the elimination of other effects from consideration.

- 8) The final loss of the sample was due to a combination of weakening of the sound field and the attractive force of acoustic streaming when the sample neared the cage.
- 9) The final, rapid motion of the sample was a wetting effect after the molten sample contacted the cage.

C. Recommendations

The following recommendations are made:

- 1) Reduce the input of water vapor to the sound field during and after injection. This could be accomplished by purging the package with dry air prior to flight and sealing it, or by preheating the sample and injector during flight to 800 degrees C.
- 2) Expand the cage so that it is outside the range of the restoring force of the sound field. This will insure that the sample will not be drawn to the cage by acoustic streaming unless it is first lost from the sound field.
- 3) Provide a second view of the sample so that three-dimensional motion can be reconstructed. This should be accomplished by a mirror arrangement and composite photographs using a single camera.
- 4) Use color film to increase contrast.
- 5) Check the injector design in the laboratory to assure that it does not significantly distort the sound field, or plan for the distortion.
- 6) Test the experiment package on one or more KC-135 flights exactly as it is to be flown on a SPAR flight. This test should include an analysis of the motion similar to the one in this report, so as to give an accurate prediction of the gross features over the longer period of time on a SPAR flight.

REFERENCES

1. King, L. V.: On the acoustic radiation pressure on spheres. Proc. Roy. Soc. (London) A147, 212-240 (1934).
2. Oran, W. A.; Berge, L. H.; and Parker, H. W.: Parametric study of an acoustic levitation system. Rev. Sci. Instrum. 51, 626-631 (1980).
3. Goldstein, H.: Classical Mechanics. 2nd ed., Addison-Wesley, Reading, Mass., 1980, pp. 88, 93, 531.
4. Symon, K. R.: Mechanics. 3rd ed. Addison-Wesley, Reading, Mass., 1971, pp. 92, 130.
5. Prandtl, L.: Essentials of Fluid Dynamics. Hafner, New York, 1952, pp. 56, 71, 176, 191.
6. Zerembo, L. K.: Acoustic Streaming. In L. D. Rozenberg, ed., High Intensity Ultrasonic Fields.
7. Lighthill, J.: Acoustic Streaming. J. Sound Vib. 61, 391-418 (1978).
8. Beyer, R. T.: Radiation pressure--The history of a mislabeled tensor. J. Acoust. Soc. Am. 63, 1025-1030 (1978).
9. Borisov, Yu. Ya. and Statnikov, Yu. G.: Flow currents generated in an acoustic standing wave. Soviet Physics-Acoustics 11, 28-33 (1965).

APPENDIX A

The sample used in the flight experiment was reported by Dr. Ralph Happe of Rockwell to be composed of gallia (41 percent), calcia (36 percent, and silica (23 percent), where percentages are mole-percentages. Mass was reported to be 0.595 gm. Measurements of sample diameter and density were unavailable. These were computed as shown below from densities of the components as reported in the Handbook of Chemistry and Physics.

densities:

$$\text{gallia} - 5.88 \text{ gm/cm}^3$$

$$\text{calcia} - 3.30 \text{ gm/cm}^3$$

$$\text{silica} - 2.20 \text{ gm/cm}^3$$

Define: N_A , N_B , N_C as the mole fractions of gallia, calcia, and silica, respectively, and M_A , M_B , and M_C as the molecular weights. Similarly, define C_A , C_B , and C_C to be the weight fractions of the respective components. Then:

$$C_A = \frac{N_A M_A}{N_A M_A + N_B M_B + N_C M_C}$$

$$C_A = \frac{(0.41)(188)}{(0.41)(188) + (0.36)(56) + (0.23)(60)} = \frac{77.08}{111.04} = 0.694$$

$$C_B = \frac{(0.36)(56)}{111.04} = 0.182$$

$$C_C = \frac{(0.23)(60)}{111.04} = 0.124$$

The density of the sample is given by

$$\frac{1}{\rho_{ABC}} = \frac{C_A}{\rho_A} + \frac{C_B}{\rho_B} + \frac{C_C}{\rho_C},$$

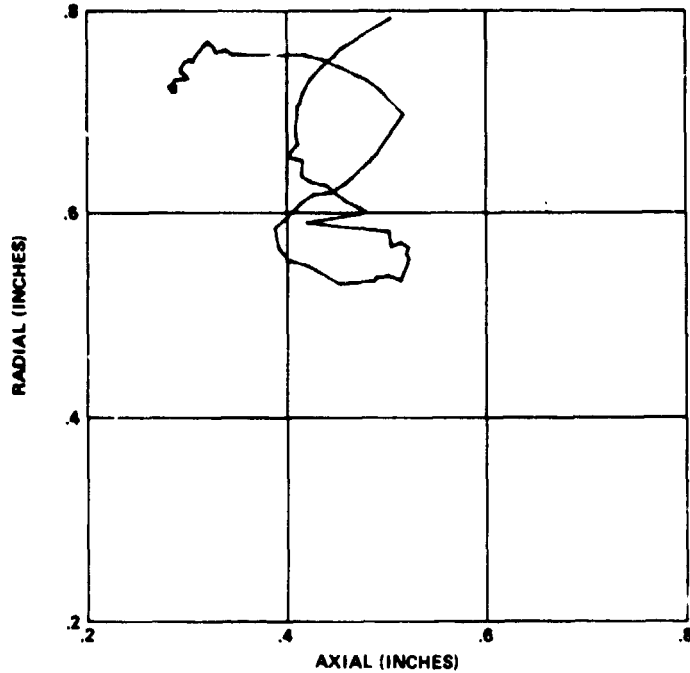
where ρ_A , ρ_B , and ρ_C are the densities of gallia, calcia, and silica, respectively.

$$\frac{1}{\rho_{ABC}} = \frac{.694}{5.88} + \frac{.182}{3.30} + \frac{.124}{2.20} \qquad \rho_{ABC} = 4.43 \text{ gm/cm}^3$$

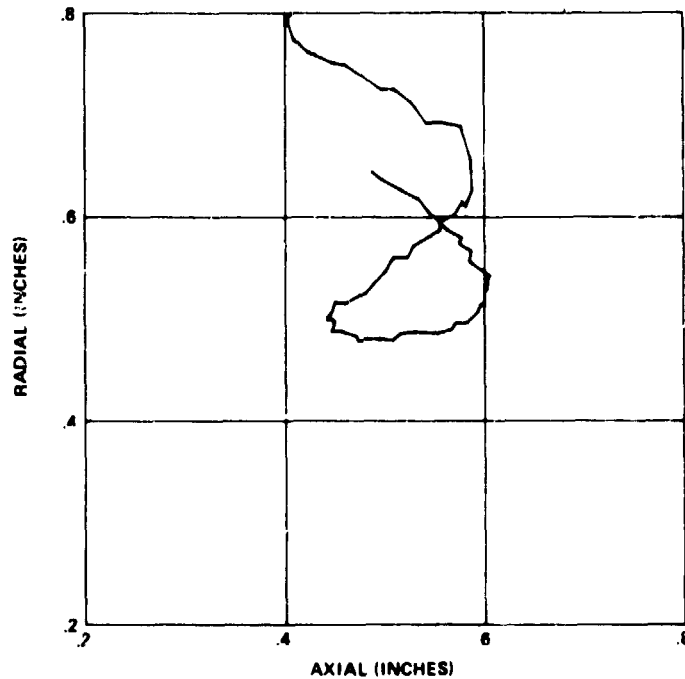
From the sample density and weight, the sample radius is calculated to be 0.318 cm, or 0.250 in.

APPENDIX B

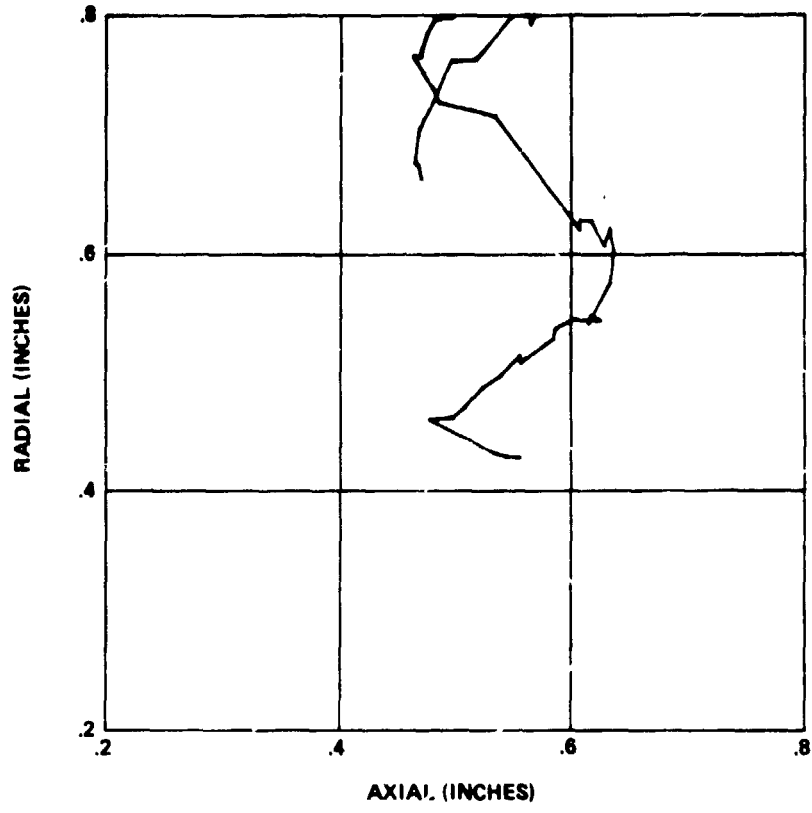
The projection of sample trajectory onto the y-z plane is shown in the series of plots in Figures B-1 through B-20. Each plot represents position data from 100 consecutive motion picture frames, or approximately 4.17 sec of data. Each plot, then, contains approximately two-thirds of a radial period and approximately two axial periods (on the average).



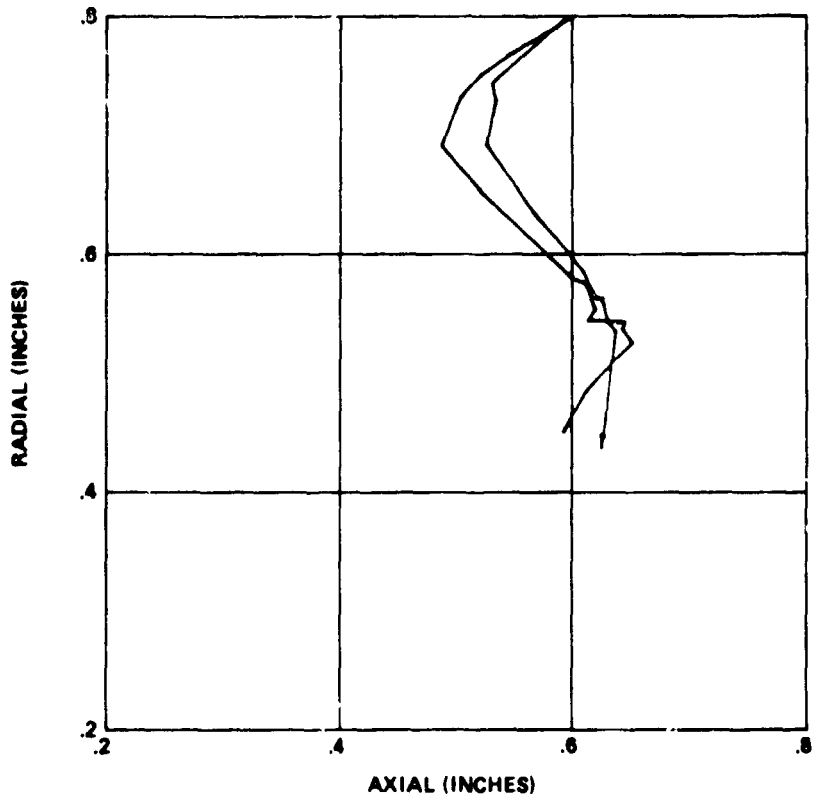
B-1. Sample trajectory for time $t = 4.21$ to 8.34 sec.



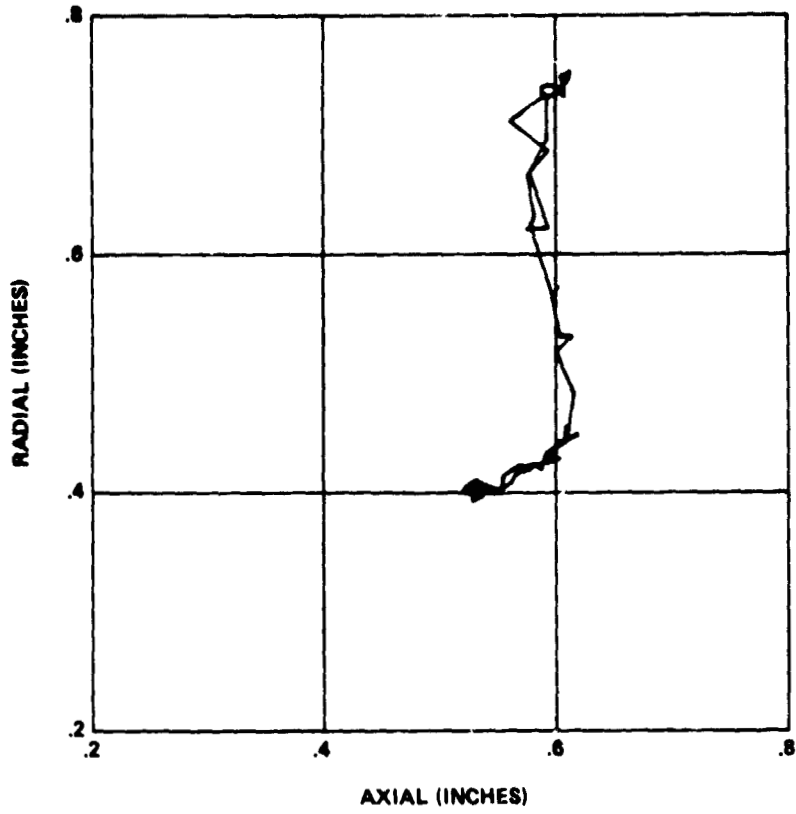
B-2. Sample trajectory for time $t = 8.38$ to 12.50 sec.



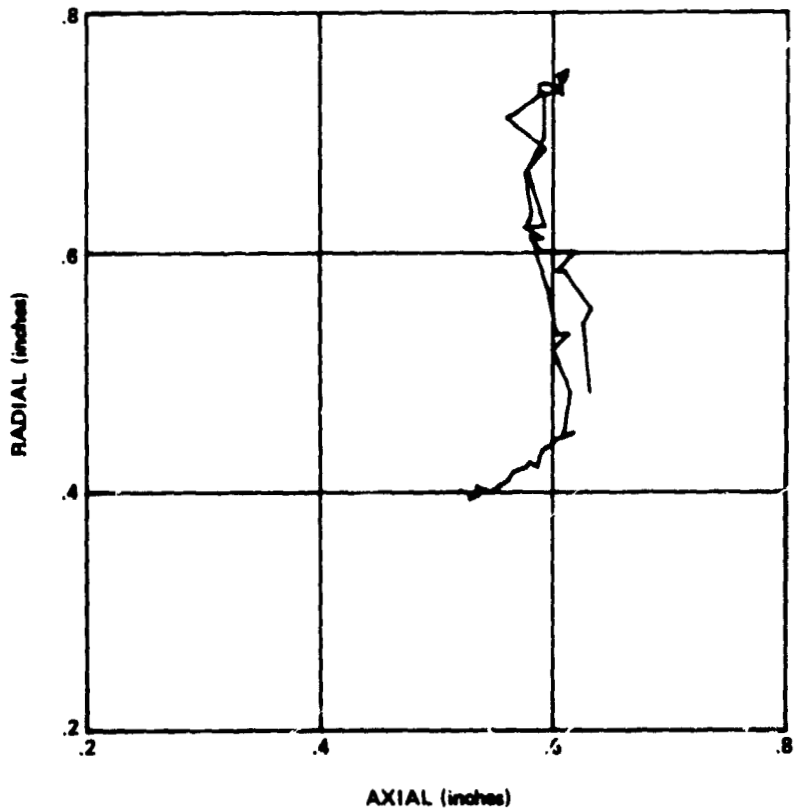
B-3. Sample trajectory for time $t = 12.55$ to 16.68 sec.



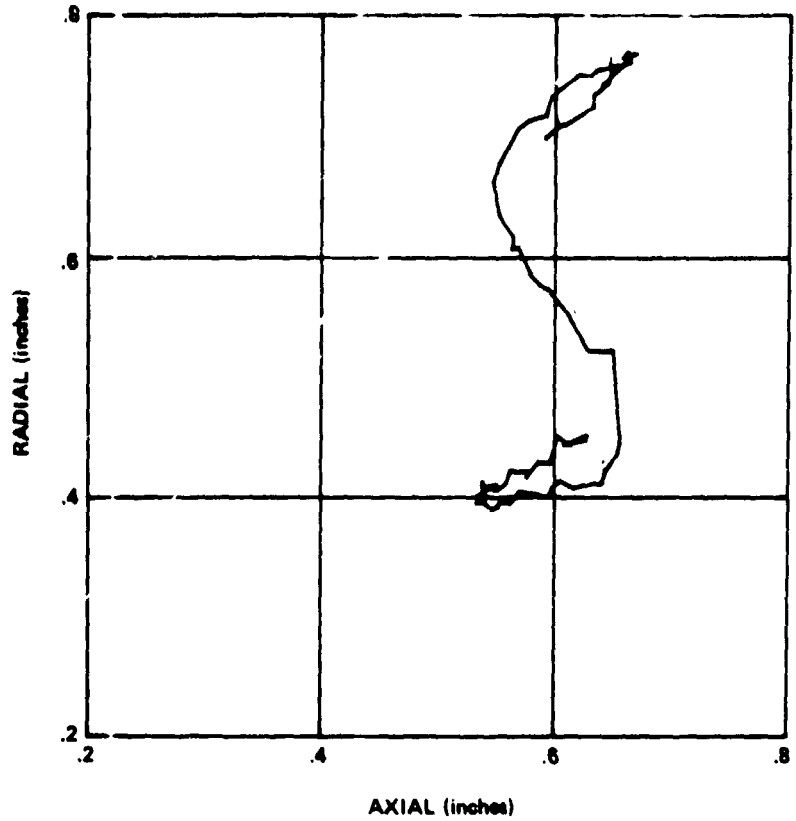
B 4. Sample trajectory for time $t = 16.72$ to 20.81 sec.



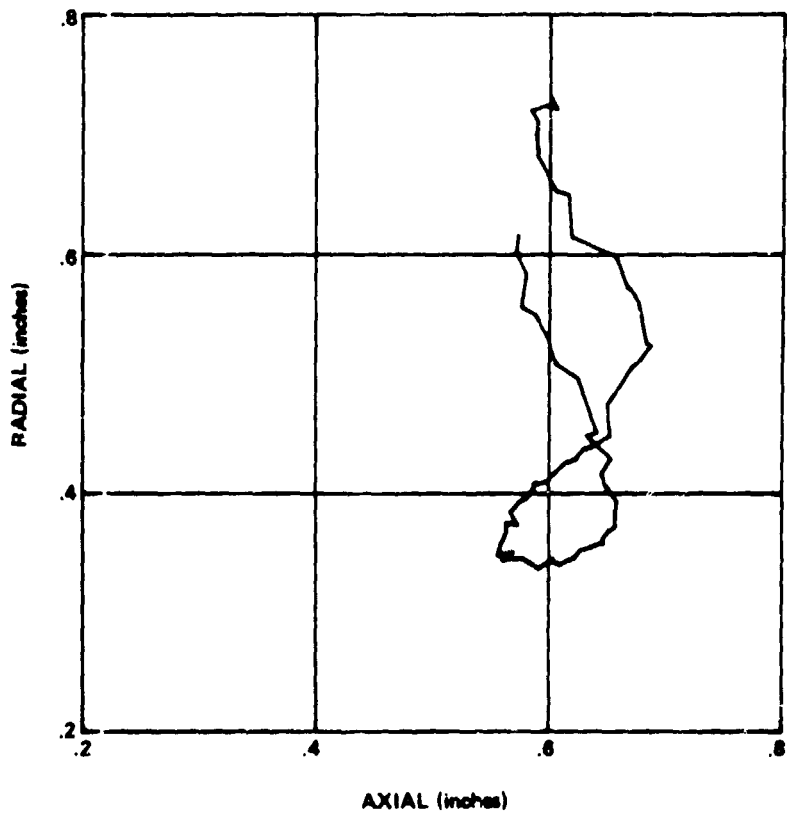
B-5. Sample trajectory for time $t = 20.85$ to 24.98 sec.



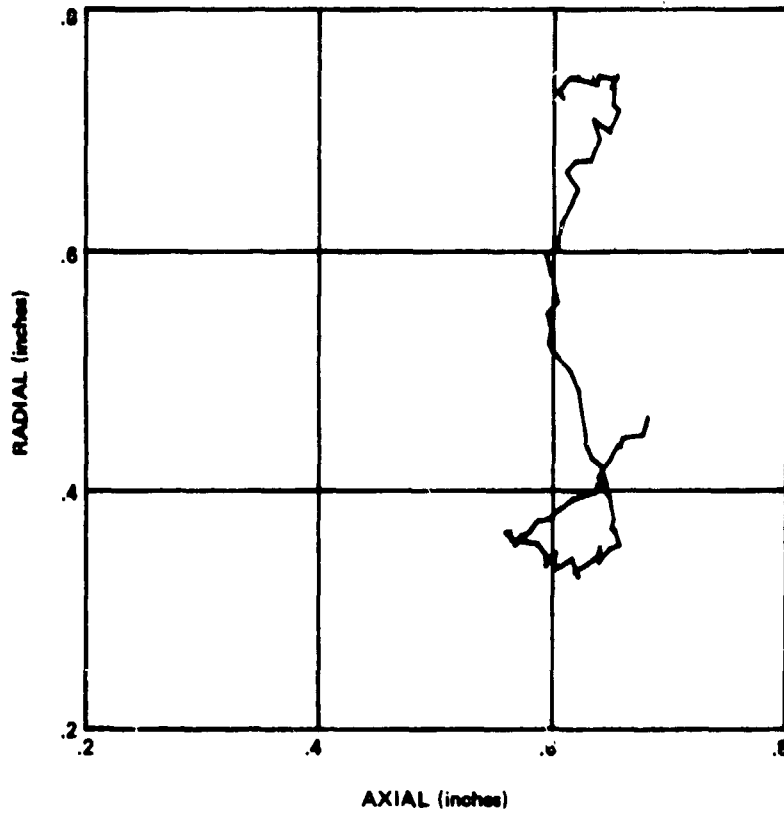
B-6. Sample trajectory for time $t = 25.02$ to 29.15 sec.



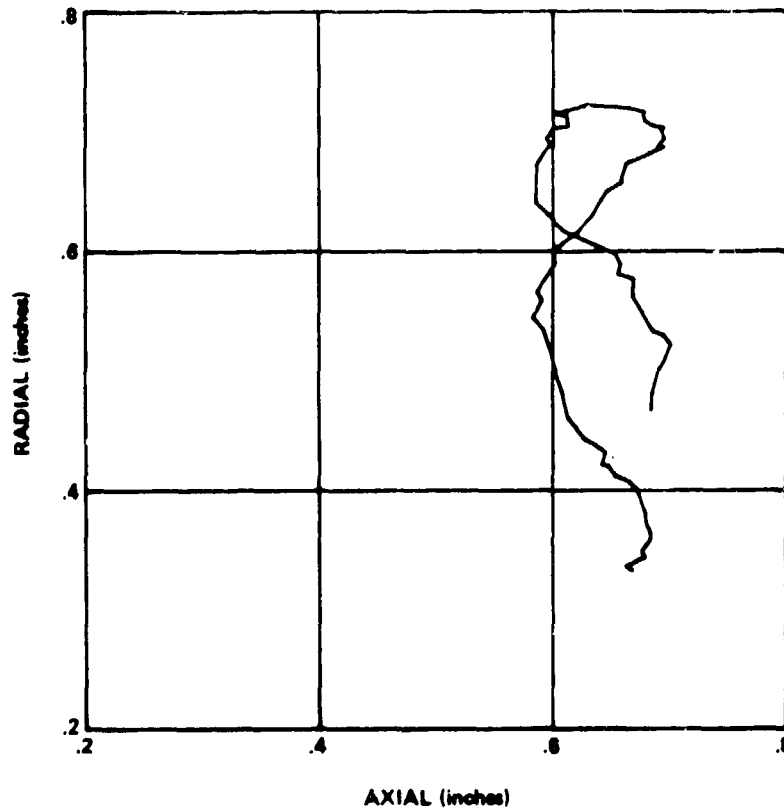
B-7. Sample trajectory for time $t = 25.71$ to 29.84 sec.



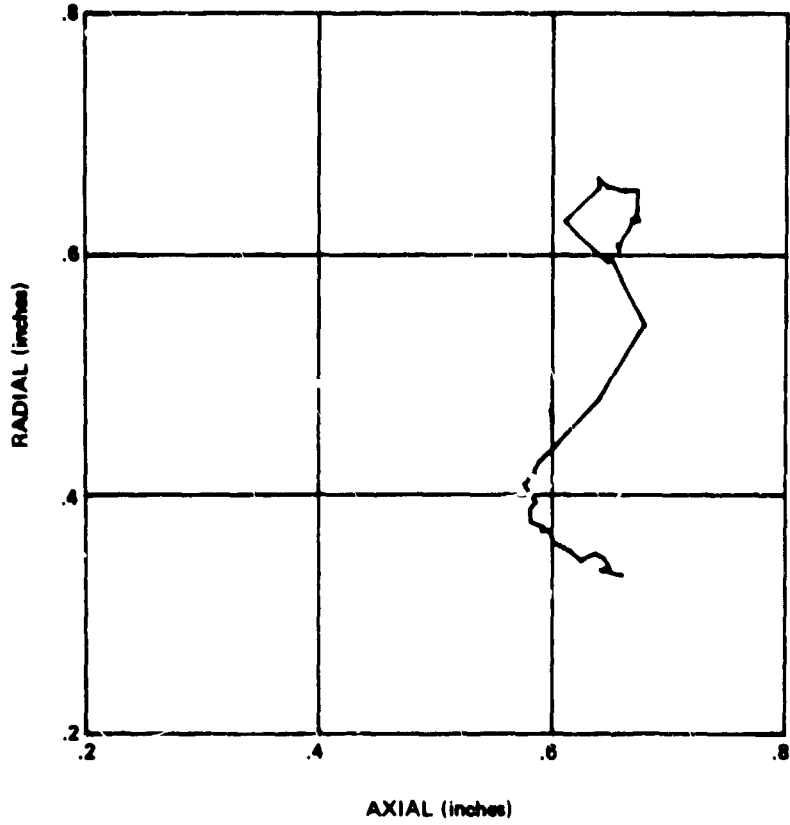
B-8. Sample trajectory for time $t = 29.88$ to 34.01 sec.



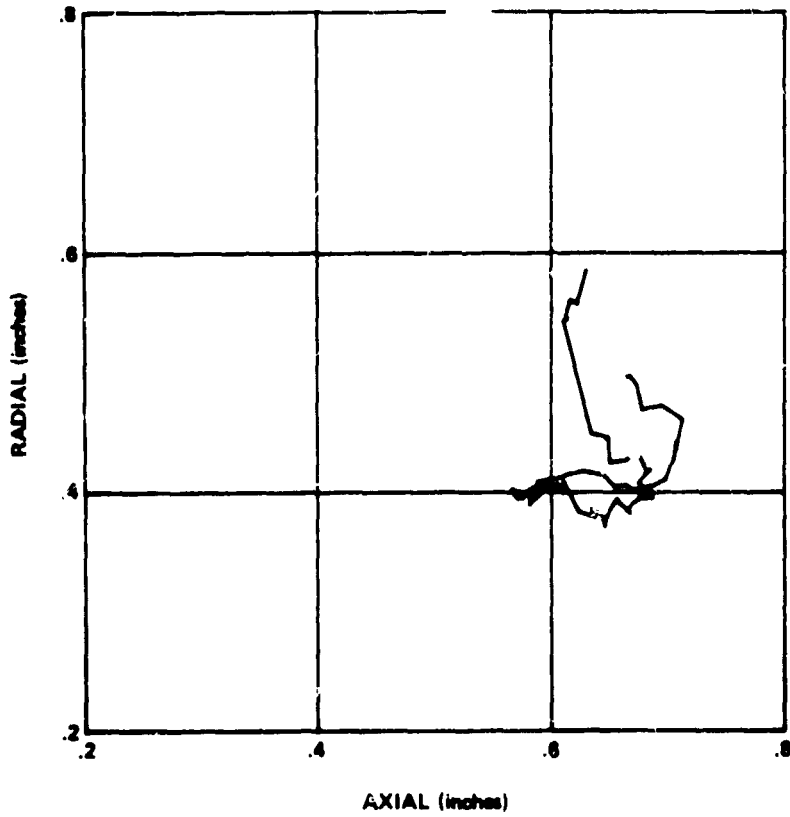
B-9. Sample trajectory for time $t = 35.05$ to 38.18 sec.



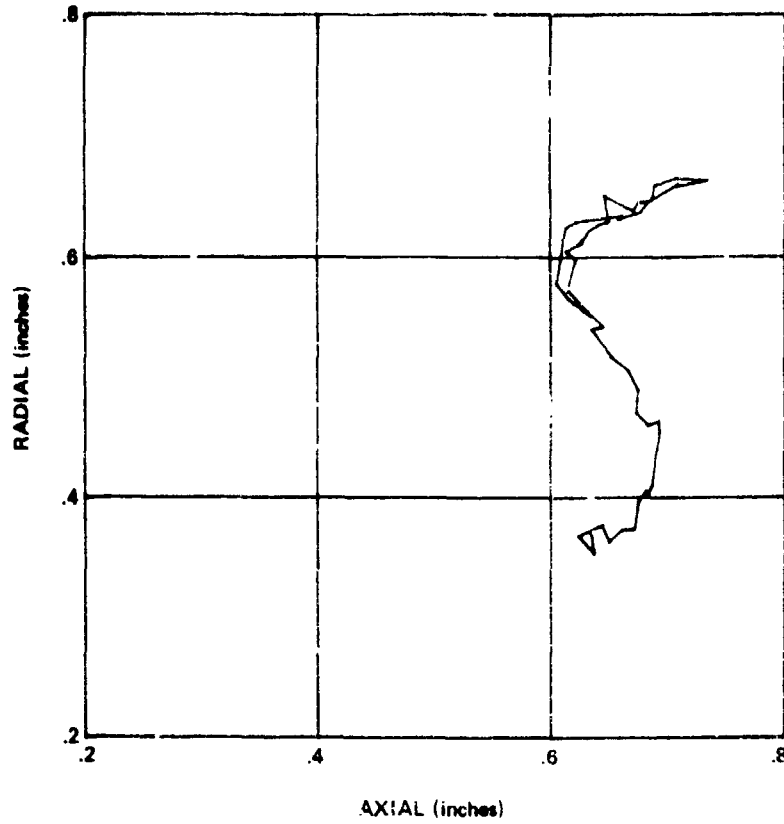
B-10. Sample trajectory for time $t = 38.22$ to 42.35 sec.



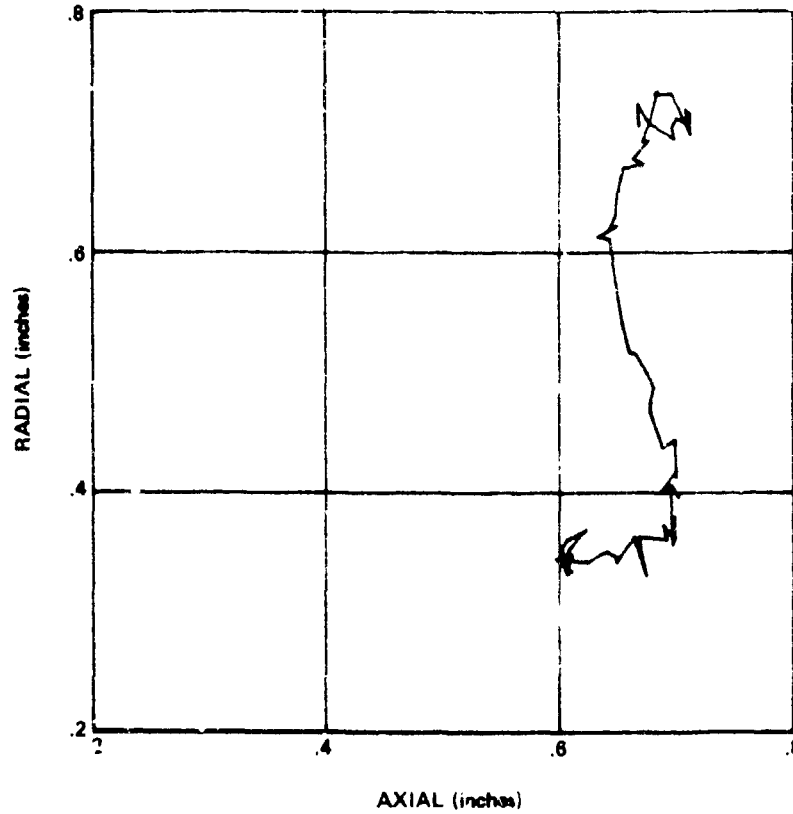
B-11. Sample trajectory for time $t = 42.39$ to 46.52 sec.



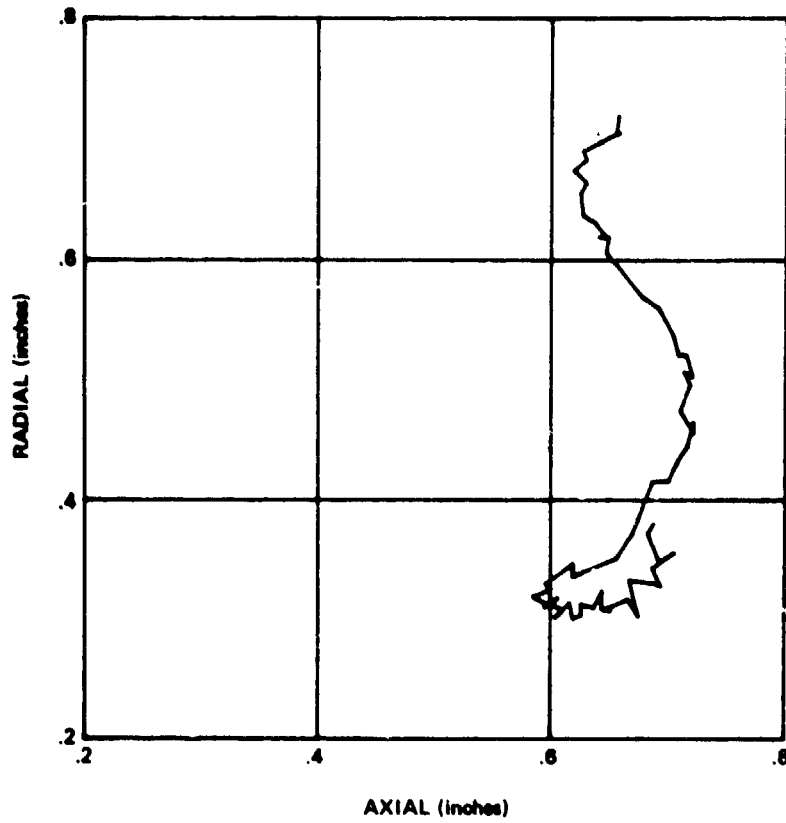
B-12. Sample trajectory for time $t = 46.56$ to 50.69 sec.



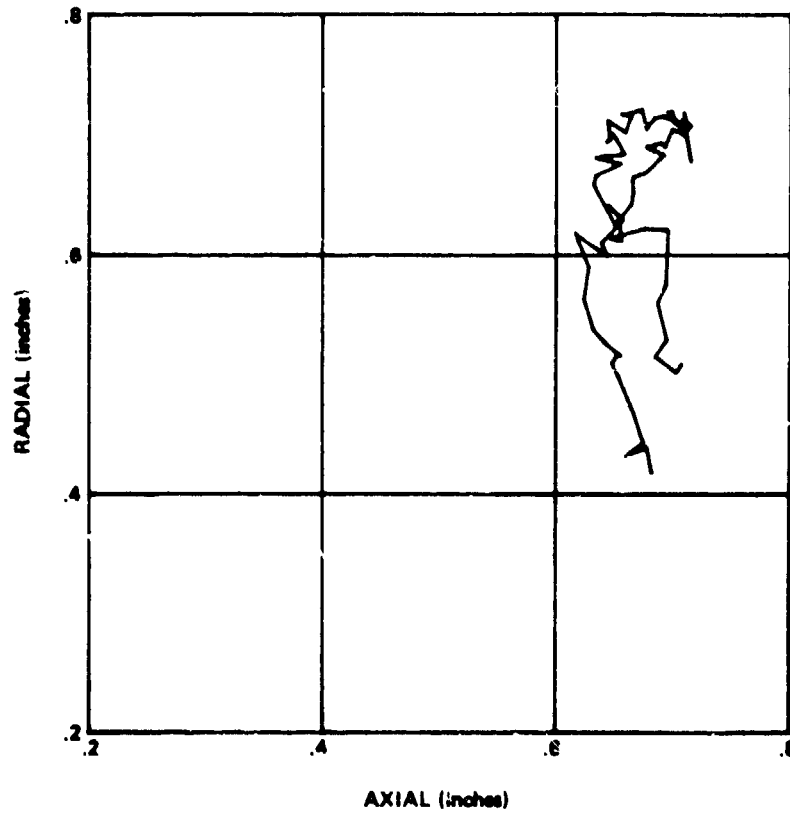
B-13. Sample trajectory for time $t = 50.73$ to 54.86 sec.



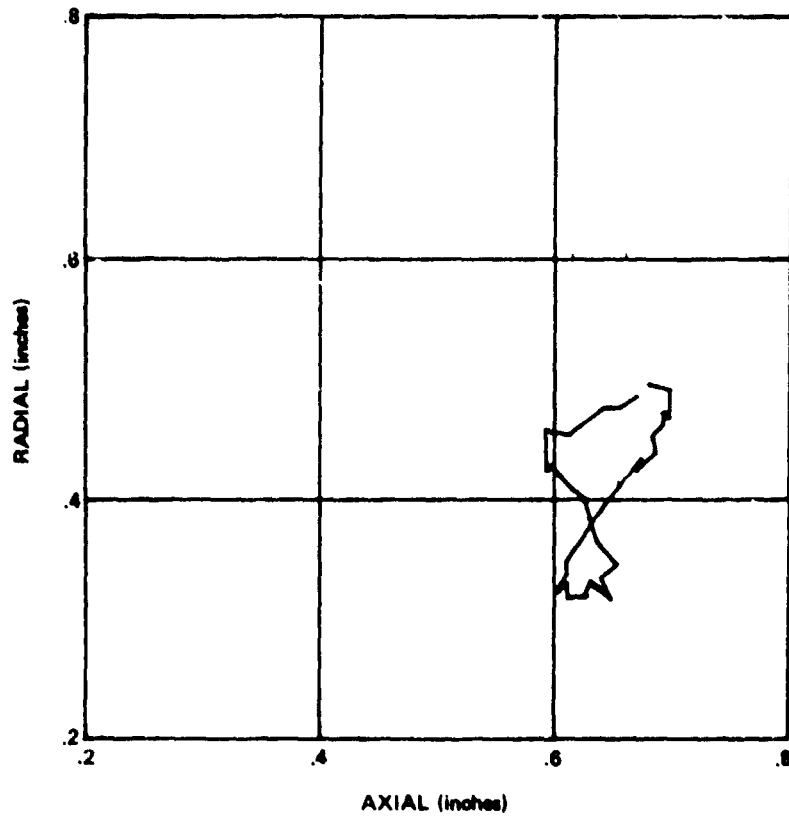
B-14. Sample trajectory for time $t = 54.98$ to 59.03 sec.



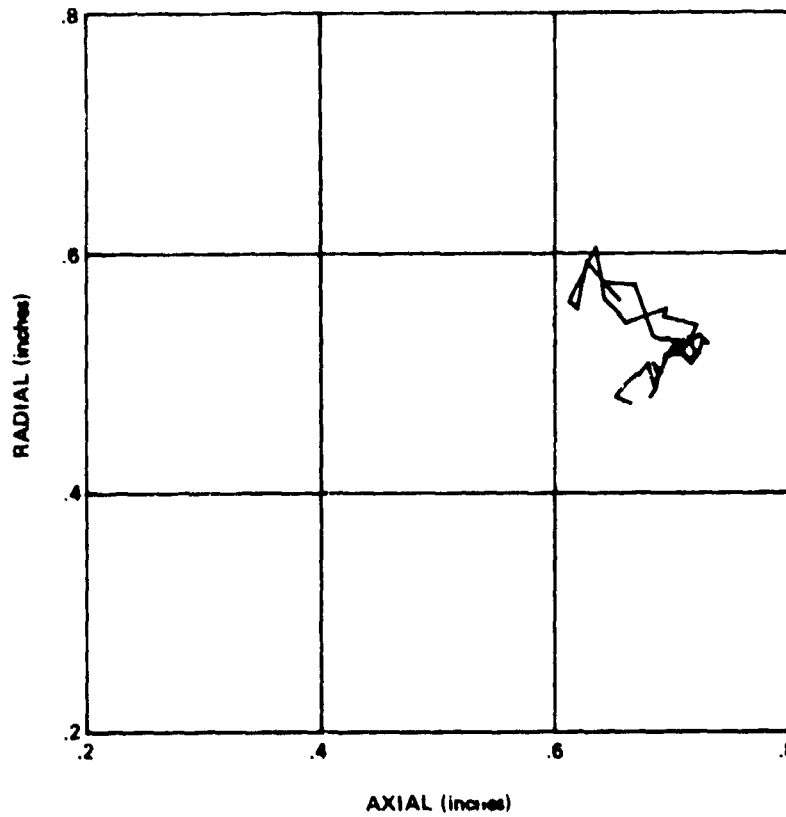
B-15. Sample trajectory for time $t = 59.07$ to 63.20 sec.



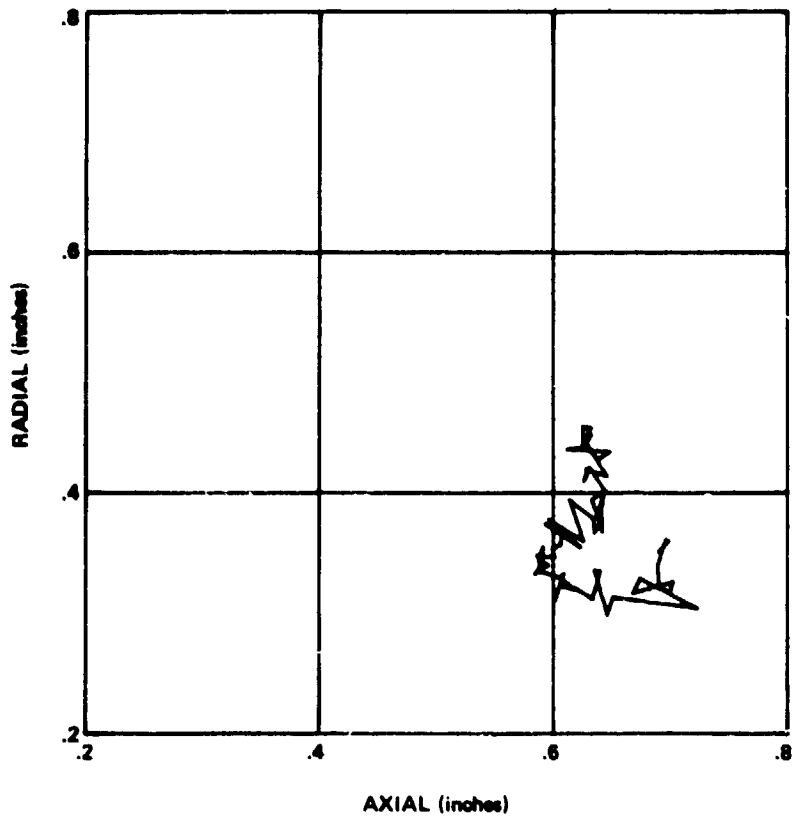
B-16. Sample trajectory for time $t = 63.24$ to 67.37 sec.



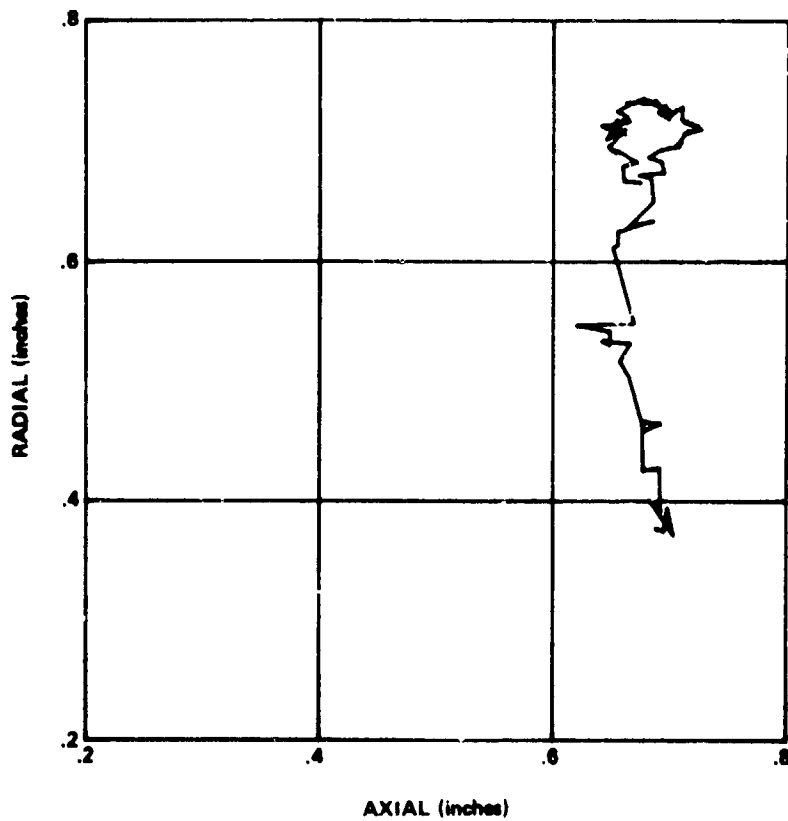
B-17. Sample trajectory for time $t = 67.41$ to 71.54 sec.



B-18. Sample trajectory for time $t = 71.58$ to 75.71 sec.



B-19. Sample trajectory for time $t = 75.75$ to 79.88 sec.



B-20. Sample trajectory for time $t = 79.92$ to 84.05 sec

APPENDIX C

The sample is observed to move a distance approximately equal to its radius in a time less than 1/24 sec; that is, the sample moved that distance between successive motion picture frames with the camera operating at 24 frames per sec. After this motion, the sample position remained fixed. The interpretation placed on this is that the sample contacted the wire cage and, because of capillary forces, flowed around a wire and remained centered on the wire because of these forces.

The force required to uniformly accelerate a mass over a distance d in a time t is given by:

$$f = m \left(\frac{2d}{t^2} \right);$$

for this sample:

$$f = (0.595 \text{ gm.}) \left\{ \frac{(2)(0.318 \text{ cm})}{(1/24 \text{ sec})^2} \right\}$$

$$f = 218 \text{ dynes.}$$

The acceleration of the sample is:

$$a = \frac{f}{m} = \frac{218 \text{ dynes}}{0.595 \text{ gm}} = 366 \text{ cm/sec}^2.$$

In terms of g , this is:

$$a = \frac{366}{980} g = 0.37 g.$$

This acceleration is too high to come from any available source except surface tension.

APPENDIX D

An approximation of the drift in the average radial position of the sample as a function of time is given by:

$$R = 475 + 285 e^{-0.035 t} ,$$

where R is the sample average position in thousandths of an inch. A plot of this function is shown in figure D-1. Similarly, an approximation for the average axial position as a function of time is given by:

$$A = 800 - 350 e^{-0.0553 t} .$$

This is shown in Figure D-2.

If we make linear approximations to the radial and axial force constants (from Figures 24 and 29), we may write

$$K_R = 1.10 - 0.0095 t$$

and

$$K_A = 11.0 - 0.095 t ,$$

where K_R and K_A have units of dynes/cm or gm/sec².

If we assume that the drift in the sample average position is due to some external force superimposed on the acoustic field, we may use the expressions for R, A, K_R , and K_A to compute these forces as functions of time. They may be expressed as:

$$F_R = K_R \Delta R$$

and

$$F_A = K_A \Delta A .$$

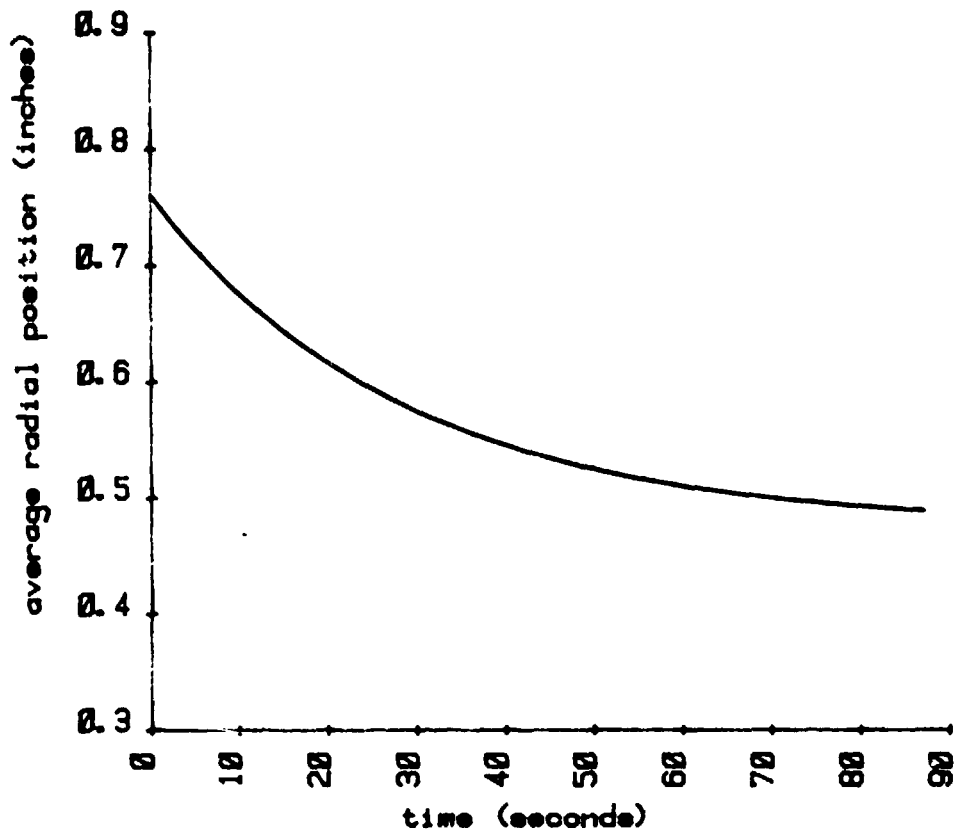


Figure D-1. Average radial position as a function of time.

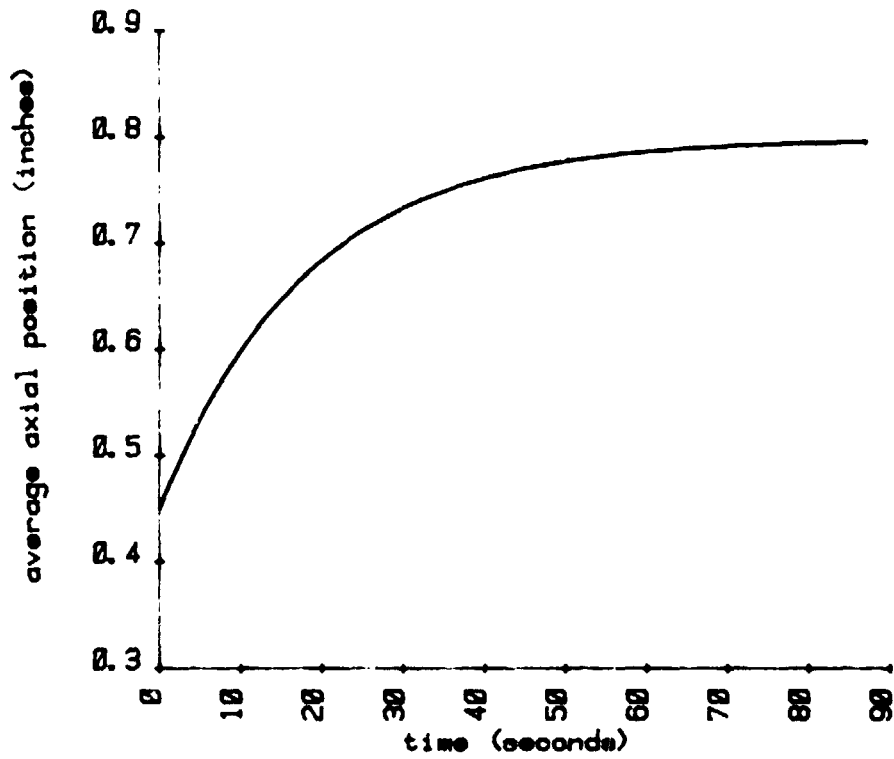


Figure D-2. Average axial position as a function of time.

Converting R and A to cgs units, we have:

$$F_R = [2.54 \times 10^{-3}][1.1 - 0.0095 t][285 (1 - e^{-0.035t})]$$

and

$$F_A = [2.54 \times 10^{-3}][11.0 - 0.095t][350 (e^{-0.0553t} - 1)] .$$

These forces are plotted in Figures D-3 and D-4, respectively.

To compare the magnitudes of these forces to others operating in the system, it is convenient to normalize them with respect to gravitational forces. In terms of g, the accelerations a mass m would undergo because of these forces are:

$$a_R = \frac{F_R}{m} \left(\frac{\xi}{980 \text{ cm/sec}^2} \right)$$

and

$$a_A = \frac{F_A}{m} \left(\frac{g}{980 \text{ cm/sec}^2} \right) .$$

For the sample with $m = 0.595 \text{ gm}$, we have:

$$a_R = (0.0017 F_R) g$$

and

$$a_A = (0.0017 F_A) g .$$

From Figures D-3 and D-4, these have values of approximately $10^{-4} g$ and $10^{-3} g$, respectively. Since these values are so high (1 to 2 orders of magnitude greater than measured values), we can conclude that the observed drifts in average sample positions do not arise from external forces. They must be due to changes in the acoustic field itself.

ORIGINAL PAGE IS
OF POOR QUALITY

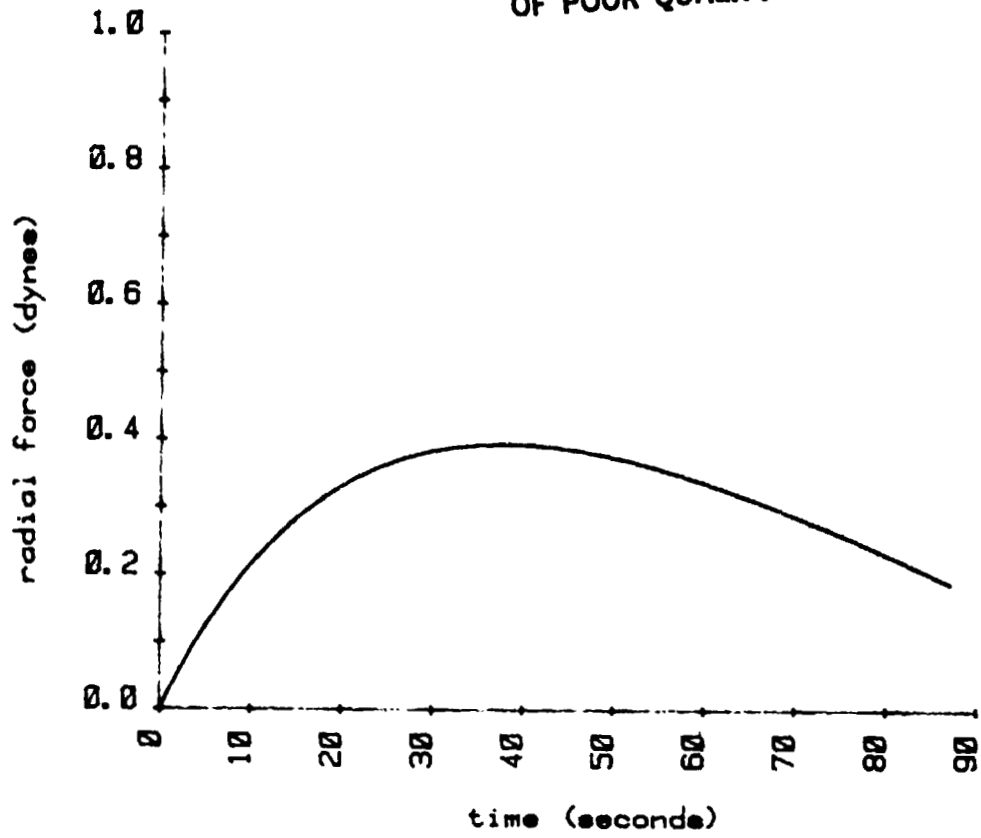


Figure D-3. Apparent radial force.

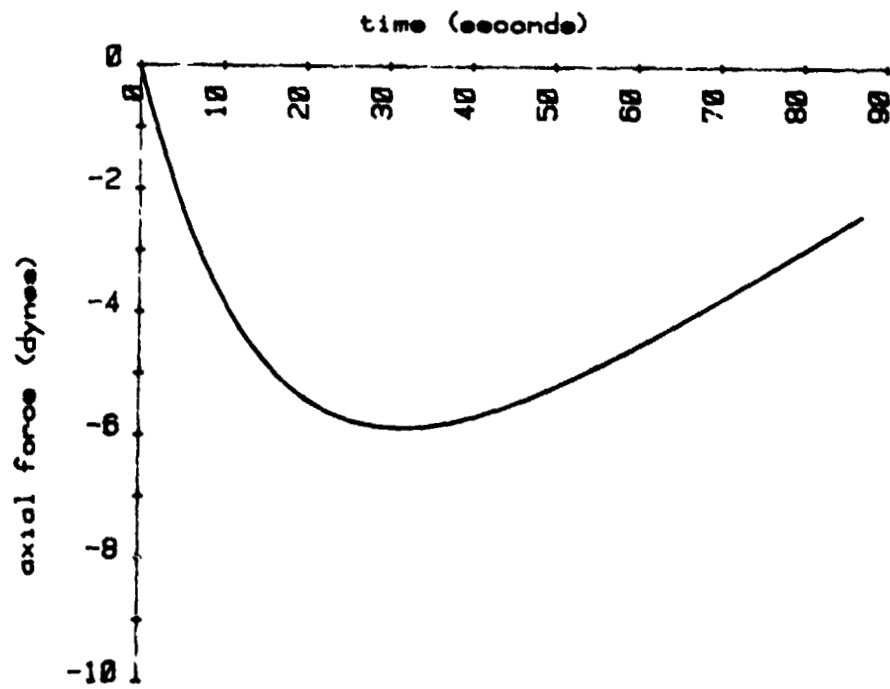



Figure D-4. Apparent axial force.

APPROVAL


ANALYSIS OF SPAR VIII SINGLE-AXIS
LEVITATION EXPERIMENT

J. E. Rush, C. F. Schafer, and R. L. Holland


The information in this report has been reviewed for technical content. Review of any information concerning Department of Defense or nuclear energy activities or programs has been made by the MSFC Security Classification Officer. This report, in its entirety, has been determined to be unclassified.



GEORGE H. FICHTL
Chief, Fluid Dynamics Branch



WILLIAM W. VAUGHAN
Chief, Atmospheric Sciences Division



for J. E. KINGSBURY
Acting Director, Space Sciences Laboratory